Role of electrostriction on domain switching near the morphotropic phase region in a ferroelectric solid solution: Thermodynamic analysis and phase-field simulations

Soumya Bandyopadhyay [1,2,*] Vaishnavi S. M. [2] Tushar Jogi [2,3] Ranjith Ramadurai [2,†] and Saswata Bhattacharyya [2,‡]

[1]*Department of Materials Science and Engineering, Indian Institute of Technology Kanpur, Kanpur-208016, India*

[2]*Department of Materials Science and Metallurgical Engineering, Indian Institute of Technology Hyderabad, Sangareddy-502285, India*

[3]*Interdisciplinary Centre for Advanced Materials Simulation (ICAMS), Ruhr-University Bochum, Germany*

(Received 22 January 2023; revised 10 August 2023; accepted 30 August 2023; published 26 October 2023)

Enhanced room-temperature electromechanical coupling in the equimolar lead-free ferroelectric solid solution of barium zirconate titanate and barium calcium titanate is attributed to the existence of an intermediate morphotropic phase region. Initial studies suggested that the existence of a polar orthorhombic phase in the morphotropic region between terminal solid solutions of rhombohedral barium zirconate titanate and tetragonal barium calcium titanate causes this enhancement. However, recent experiments suggest the coexistence of two or more of these phases in the morphotropic region. Such coexistence can often arise due to changes in anisotropy in electrostriction. To understand the effect of anisotropy in electrostriction on the stability of these phases and the consequent polarization switching characteristics in the equimolar solid solution, we performed systematic phase-field simulations of domain evolution to the steady state in this system under stress-free conditions as a function of anisotropy in electrostriction defined by $Q_z = 2Q_{44}/(Q_{11} - Q_{12})$, where Q_{11}, Q_{12}, and Q_{44} are the independent coefficients of the electrostriction tensor (expressed using Voigt notation). Our results show a systematic reduction in polarization anisotropy with increasing Q_z. For example, a single-phase configuration consisting of orthorhombic variants corresponding to isotropic electrostrictive moduli ($Q_z = 1$) transforms to a three-phase configuration containing tetragonal, orthorhombic, and rhombohedral variants when the moduli show strong anisotropy ($Q_z = 2.5$). We use the effective in-plane and out-of-plane piezoelectric coefficients and their ratio as a measure of the electromechanical switching characteristics. Unlike polarization anisotropy behavior, these characteristics do not exhibit such monotonic behavior. The effective piezo coefficients depend not only on the number of coexisting polar phases but also on their spatial configuration with respect to the applied field. Our predictions pertaining to the coexistence of tetragonal and orthorhombic variants and the corresponding effective out-of-plane piezoelectric coefficient show good agreement with experimental findings. We also discuss how clamped or constrained conditions can modify the phase stability observed under stress-free conditions.

DOI: 10.1103/PhysRevB.108.134116

I. INTRODUCTION

One of the key challenges in the field of oxide-based electronics is the development of environment friendly lead-free ferroelectrics that can replace the high-performance lead-based counterparts, such as lead zirconate titanate (PZT) and lead magnesium niobate - lead titanate (PMN-PT) systems [1–4]. Although several lead-free ferroelectric systems have been identified in the last decade, attaining a room-temperature piezoresponse superior to the best available lead-based system is still a challenge [5–7].

There is renewed interest in barium titanate (BTO), the first discovered perovskite ferroelectric with perfect cubic perovskite structure (ABO_3 with point group $m\bar{3}m$) above 120 °C, which transforms to tetragonal $4mm$ symmetry at room temperature [2,8]. However, the piezoresponse of undoped bulk BTO at room temperature, characterized by electromechanical coupling coefficients d_{33} and d_{31}, is far lower than that of PZT. Therefore there are continuing efforts to improve the electromechanical coupling efficiency or piezoresponse of BTO at room temperature using a combination of doping, nanostructuring, and strain-tuning [8–18].

Recently, a new BTO-based solid solution with zirconium-doped BTO and calcium-doped BTO as the two components [chemical formula: $(1-x)Ba(Zr_{0.2}Ti_{0.8}O_3)$-$x(Ba_{0.7}Ca_{0.3})TiO_3$ ($0 \leqslant x \leqslant 1$), abbriviated as BZCT] has emerged as one of the most promising lead-free ferroelectric for electromechanical applications at room temperature. The highest piezoresponse of equimolar ($x = 0.5$) BZCT at room temperature is around 620 pC N^{-1}, which exceeds that of PZT [13–16]. Moreover, structural studies of BZCT and PZT reveal a unique similarity in thermodynamic characteristics—both show morphotropic phase transition below their Curie temperatures at or around the equimolar composition [19–21].

*bsoumya@iitk.ac.in
†ranjith@msme.iith.ac.in
‡saswata@msme.iith.ac.in

The morphotropic phase region (MPR) bounded by morphotropic phase boundaries (MPB) is a region of high electromechanical activity and consists of an intermediate phase between the terminal solid solutions. Presence of an intermediate phase having lower crystallographic symmetry than the terminal ones introduces tetracritical points marking the coexistence of the ferroelectric phases. It also results in an increase in polarization rotation by reducing the energy barrier for transition between the phases. Moreover, lower crystallographic symmetry of the intermediate phase increases the number of polar variants which are also ferroelastic. Thus there is an enhancement of strain accommodation within the MPR that softens effective elastic moduli of the ferroelectric thereby increasing the effective electromechanical moduli [22,23].

Although initial structural studies of BZCT described the MPB as a region of coexistence of $R + T$ [13,24], Keeble *et al.* used high-resolution synchrotron x-ray diffraction to characterize the structure of BZCT for the entire range of compositions ($0 \leqslant x \leqslant 1$) and temperatures varying between 100 and 500 K to reveal an intermediate phase region with orthorhombic symmetry for the composition range ($0.45 < x < 0.55$) at room temperature [25]. However, there exists uncertainty in determining phase stability within this intermediate region (MPR) even at the room temperature [26–28].

Brajesh *et al.* implemented a powder poling technique to study electric field induced structural transformations in BZCT at the MPB. Structural analysis of poled BZCT powder using x-ray diffraction and Rietveld refinement showed the coexistence of T, O, and R phases for the morphotropic composition range ($0.45 < x < 0.55$) at room temperature [26]. Later, they showed a stress-induced ferroelastic transformation above the Curie temperature preceding the ferroelectric to paraelectric transformation in equimolar BZCT. In order to relieve the stress associated with high-temperature ferroelastic transformation, BZCT samples were annealed at 400 °C (which is well above $T_c = 120\,^{\circ}\mathrm{C}$). Subsequently, they observed a change in phase coexistence where the amount of R reduced significantly with a corresponding increase in the fractions of T and O [27]. These studies suggest appreciable structural distortion in the oxygen octahedra during processing, which is responsible for higher electrostrains near MPB. The presence of higher electrostrains can notably alter the phase stability.

Since, coefficients of electrostriction are inherently related to oxygen octahedral structure in perovskite oxides of the form ABO_3, electromechanically induced phase transition in these will lead to distortion of oxygen octahedra often resulting in anisotropic electrostrictive coefficients [29]. Since electrostrictive coefficients couple spontaneous strain and spontaneous polarization, change in electrostriction will alter the free energy of ferroelectrics leading to change in thermodynamic stability of polar phases [30].

It should be noted that the physical properties of the parent paraelectric phase with cubic crystal structure that are represented by fourth rank or higher "even" rank tensors, such as electrostriction (Q_{ijkl}) or elasticity (C_{ijkl}), can show cubic anisotropy at the most (Neumann's principle) [31]. For example, bulk barium titanate and lead-based perovskite solid solutions show large cubic anisotropy at room temperature when the anisotropy parameter is defined as $Q_a = \frac{Q_{11}-Q_{12}}{Q_{44}} > 1$, where Q_{11}, Q_{12}, Q_{44} are the independent electrostrictive coefficients [29]. Note that, here we use Voigt notation to represent a symmetric tensor by reducing its order, such as $Q_{ijkl} \rightarrow Q_{\alpha\beta}$ [32]. Moreover, the change in anisotropy in spontaneous strain during the paraelectric-to-ferroelectric transition can affect the switching behavior of perovskite ferroelectrics manifested in large differences between the measured transverse (d_{31}) and longitudinal (d_{33}) piezocoefficients [29,33–35].

To relate stability of polar domains and domain dynamics with electromechanical switching properties of BZCT solid solution, we require a thermodynamic potential integrated with elastic and electrostatic interactions which can not only predict the stability of polar phases in the stress-free, electrically neutral state as a function of temperature and composition, but can also capture changes in phase stability with application of electromechanical loading [36,37]. There have been extensive efforts to develop thermodynamic potentials of ferroelectric solid solutions. Here we list the most significant ones. Cao and Cross made the first attempt to develop a thermodynamic description of a ferroelectric solid solution where they combined the classical Ginzburg-Landau-Devonshire formalism for ferroelectrics with a regular solution model describing interactions between the components of the ferroelectric system [38]. Later, Bell and Furman modified the regular-solution term and included additional coupling between polarization order parameters and Landau free energy coefficients [39]. The modified model could successfully describe phase coexistence at the MPB of PZT. Li *et al.* made further modifications to the thermodynamic potential using a single order parameter free energy for the entire composition range and introduced composition- and temperature-dependent Landau coefficients [40]. The model was used to study ferroelectric/ferroelastic domain evolution in epitaxially grown PZT films. Later, Heitmann and Rossetti developed a generalized thermodynamic model for ferroelectric solid solutions containing MPB/MPR, wherein they incorporated direction-dependence of polarization field and described Landau polynomial in terms of isotropic and anisotropic polarization components [41]. Since MPB defines the coexistence of low-symmetry phases marked by vanishing polarization anisotropy at the tricritical points, their model could accurately predict both location and shape of MPBs in several lead-based and lead-free solid solutions [37]. Yang *et al.* [42] developed a thermodynamic potential for BZCT based on the polar anisotropy theory of Heitmann and Rossetti [37,41]. Although the model could predict the stability of orthorhombic phase within MPR of BZCT around the equimolar composition, it does not show correspondence with the phenomenological Landau-Ginzburg-Devonshire (LGD) theory and does not correlate stability of polar domains with electromechanical response.

Since ferroelectric phases are inherently ferroelastic, accurate prediction of phase stability requires coupling of electrostatic and elastic interactions. Recently Huang *et al.* [43] developed a thermodynamic potential for barium zirconate titanate (BZT) including coupling between electrostatic and

elastic interactions that showed excellent agreement with experimental phase stability data. Here, we build upon the thermodynamic potential proposed by Yang *et al.* [42] to develop a free energy based on LGD formalism [37] to study phase stability, evolution of polar domains and polarization switching behavior in BZCT. To understand the role of electromechanical anisotropy on polar domain stability and polarization switching in BZCT, we introduce a parameter $Q_z = 2Q_{44}/(Q_{11} - Q_{12})$ in a similar sense to Q_a. Furthermore, we systematically vary Q_z to investigate domain evolution within MPR and the resulting electromechanical switching characteristics. In each case, we compare the effective piezoresponse coefficients, d_{33} and d_{31}, computed from the simulated phase loops, with those measured experimentally [25].

The paper is organized as follows. In the following section, we present our formulation where we derive a thermodynamic potential for BZCT solid solution incorporating electrostatic and elastic interactions and develop a phase-field model based on this potential to study domain evolution in BZCT under applied electromechanical fields. In the subsequent section, we present our results correlating the changes in the predicted diffusionless phase diagrams with the change in electromechanical anisotropy. We also present our results of three-dimensional phase-field simulations of domain evolution and relate them to the switching characteristics in BZCT due to applied electromechanical fields. We have compared our simulated data on phase stability and effective piezoelectric coefficients with the best available experimental measurements. Finally, we summarize the key conclusions from this study.

II. MODEL FORMULATION

We begin with the description of energetics of BZCT system using the Landau-Ginzburg-Devonshire (LGD) thermodynamic formalism. We draw equivalence between the LGD free energy and a thermodynamic potential based on the theory of polar anisotropy to derive thermodynamic criteria defining the MPBs in stress-free, electrically neutral BZCT system [37,42]. Next, we describe electrostatic, elastic and external electromechanical field contributions to the total free energy of the system and develop a three-dimensional phase-field model to study domain evolution in BZCT. The phase-field model consists of a set of Allen-Cahn equations describing the spatiotemporal evolution of the polarization order parameter field $\mathbf{P}(\mathbf{r}, t)$ coupled with an electrostatic equilibrium equation for the electric field and a mechanical equilibrium equation for the strain field. Since the model includes external field effects, it can be used to correlate domain configuration with the polarization switching characteristics. In what follows, we have used indicial notations (with Einstein summation convection) to describe vector and tensor quantities in terms of their components. Otherwise, we denote vector fields with bold letters and higher order tensor fields using standard matrix notations.

A. Thermodynamic potential

The total free energy $\mathcal{F}$ of a ferroelectric system is expressed as follows [36,44]:

$$\mathcal{F}(P_i, \varepsilon_{ij}, E_i) = \int_V (f_{\text{bulk}} + f_{\text{electric}} + f_{\text{elastic}} + f_{\text{gradient}})dV \quad (i, j = 1, 2, 3), \tag{1}$$

where f_{bulk}, f_{electric}, f_{elastic}, and f_{gradient} denote the bulk, electric, elastic and gradient energy densities, respectively. P_i are the components of the spontaneous polarization order parameter field, ε_{ij} denotes spontaneous strain field related to P_i through the third-rank piezoelectric tensor d_{ijk} and fourth rank electrostrictive tensor Q_{ijkl} with $i, j, k, l = 1, 2, 3$.

Using the unpolarized, stress-free and centrosymmetric paraelectric state (cubic) as the reference state, f_{bulk} for BZCT is expressed using a sixth-order Ginzburg-Landau polynomial:

$$\begin{aligned} f_{\text{bulk}} = {} & \tfrac{1}{2}\alpha_1\left(P_1^2 + P_2^2 + P_3^2\right) + \tfrac{1}{4}\alpha_{11}\left(P_1^4 + P_2^4 + P_3^4\right) \\ & + \tfrac{1}{6}\alpha_{111}\left(P_1^6 + P_2^6 + P_3^6\right) + \tfrac{1}{2}\alpha_{12}\left(P_1^2P_2^2 + P_2^2P_3^2 + P_3^2P_1^2\right) \\ & + \tfrac{1}{2}\alpha_{112}\left(P_1^4\left(P_2^2 + P_3^2\right) + P_2^4\left(P_3^2 + P_1^2\right) + P_3^4\left(P_1^2 + P_2^2\right)\right) \\ & + \tfrac{1}{6}\alpha_{123}P_1^2P_2^2P_3^2, \end{aligned} \tag{2}$$

where P_1, P_2, P_3 are the components of the polarization field $\mathbf{P}(\mathbf{r})$. The phenomenological Landau expansion coefficients $(\alpha_1, \alpha_{11}, \alpha_{12}, \alpha_{111}, \alpha_{112}, \alpha_{123})$ are functions of composition (x) and temperature (θ) and determine the energy of the stress-free, electroneutral state of the system. The coefficients are chosen appropriately to ensure a first-order transition ($\alpha_1 < 0$, $\alpha_{11} < 0$, $\alpha_{111} > 0$) between the paraelectric and ferroelectric states.

To derive thermodynamic stability conditions during paraelectric to ferroelectric phase transition and compute diffusionless phase diagrams of BZCT system, Eq. (2) is expressed in an alternate form based on polar anisotropy theory where we separate isotropic part of the free energy from the direction-dependent anisotropic part [37,41]. Therefore we define the spontaneous polarization field $\mathbf{P}$ as a product of the magnitude of spontaneous polarization $P = |\mathbf{P}|$ and a unit vector $\mathbf{n} = (n_1, n_2, n_3)$ along the direction of spontaneous polarization: $\mathbf{P} = \mathbf{n}P$. Thus, separating the isotropic and anisotropic parts, we rewrite the modified bulk free energy density as

$$\begin{aligned} f_{\text{bulk}}^{\text{modified}} &= f_{\text{bulk}}^{\text{iso}} + f_{\text{bulk}}^{\text{aniso}}, \quad \text{where} \\ f_{\text{bulk}}^{\text{iso}} &= \tfrac{1}{2}\alpha_1 P^2 + \tfrac{1}{4}\beta_1 P^4 + \tfrac{1}{6}\gamma_1 P^6 \\ f_{\text{bulk}}^{\text{aniso}} &= \tfrac{1}{4}\beta_2\left(n_1^4 + n_2^4 + n_3^4\right)P^4 \\ &\quad + \tfrac{1}{6}\left[\gamma_2\left(n_1^6 + n_2^6 + n_3^6\right) + \gamma_3 n_1^2 n_2^2 n_3^2\right]P^6, \end{aligned} \tag{3}$$

where $f_{\text{bulk}}^{\text{modified}}$ is the alternate form of the bulk free energy density which separates isotropic and anisotropic contributions. Note that the isotropic part of the energy describes the transition from a nonpolar phase to a polar glassy state with no preferential direction, while the anisotropic part defines the directional dependence of free energy sur-

face due to the spontaneous polarization vector [37,41]. In Eq. (3), $\beta_1 = \alpha_{12}$, $\beta_2 = \alpha_{11} - \alpha_{12}$, $\gamma_1 = \alpha_{112}$, $\gamma_2 = \alpha_{111} - \alpha_{112}$, $\gamma_3 = \alpha_{123} - 6\alpha_{112}$ are the modified Landau coefficients, respectively. The detailed derivation of obtaining the modified Landau potential is shown in Appendix A.

The electric energy density f_{electric} in Eq. (1) is given as

$$f_{\text{electric}} = -\tfrac{1}{2}\epsilon_0\epsilon_b\left(E_1^2 + E_2^2 + E_3^2\right) - (P_1E_1 + P_2E_2 + P_3E_3), \tag{4}$$

where E_1, E_2, E_3 are the components of the total electric field $\mathbf{E}(\mathbf{r})$ that comprises an internal depolarization field $\mathbf{E}^{\text{d}}(\mathbf{r})$ resulting from dipole-dipole interactions (f_{dipole}), an externally applied field $\mathbf{E}^{\text{ext}}$, and a random field $\mathbf{E}^{\text{random}}(\mathbf{r})$ associated with compositional heterogeneity of the polar solid [45]. The depolarization field $\mathbf{E}^{\text{d}}(\mathbf{r})$ is defined as [44]

$$E_i^{\text{d}}(r_k) = \frac{1}{4\pi\epsilon_0\epsilon_b}\left(\frac{P_i(r_k)}{|\mathbf{r}|^3} - \frac{[3P_j(r_k)r_j]r_i}{|\mathbf{r}|^5}\right), \tag{5}$$

where ϵ_0 is the permittivity of free space and ϵ_b denotes the background dielectric permittivity due to dielectric screening [46,47]. In the absence of external and random fields, $E_i^{\text{d}}(\mathbf{r})$ is the solution to electrostatic equilibrium equation defined as follows:

$$\nabla_i D_i = 0, \tag{6}$$

where $D_i = \epsilon_0\epsilon_b E_i^{\text{d}} + P_i$ is the electric displacement vector. We define electric energy [Eq. (4)] in accordance with "spontaneous polarization order parameter (SPOP)" approach, wherein we separate the spontaneous polarization field $\mathbf{P}(\mathbf{r})$ from the polarization $\mathbf{P}^{\text{ext}}(\mathbf{r})$ induced by the externally applied field (including dielectric screening effect) [48]. On the other hand, "total polarization order parameter (TPOP)" approach uses total polarization field $\mathbf{P}^T(\mathbf{r})$ as the order parameter where the dielectric displacement vector is defined as $D_i = \epsilon_0 E_i^d + P_i^T$. In the latter, we cannot define a background dielectric constant (ϵ_b) and the contributions to the electric energy from the external and internal fields are given separately [48]:

$$f_{\text{electric}} = -\tfrac{1}{2}P_i^T E_i^d - P_i^T E_i^{\text{ext}}. \tag{7}$$

Note that both approaches are equivalent and should yield the same electric energy density.

Since spontaneous polarization in a ferroelectric crystal is a result of displacement of ions in the lattice from the reference paraelectric state, it engenders spontaneous strain [30]. The spontaneous strain order parameter field $\varepsilon^0(\mathbf{r})$ for a stress-free crystal is defined as follows [36]:

$$\varepsilon_{ij}^0 = Q_{ijkl}P_kP_l, \tag{8}$$

where Q_{ijkl} denotes the rank-4 electrostrictive coefficient tensor.

Using the definition of stress-free strain or eigenstrain [Eq. (8)], elastic energy density f_{elastic} is defined as

$$f_{\text{elastic}} = \tfrac{1}{2}C_{ijkl}\left(\varepsilon_{ij}^T - \varepsilon_{ij}^0\right)\left(\varepsilon_{kl}^T - \varepsilon_{kl}^0\right), \tag{9}$$

where C_{ijkl} is the elastic stiffness tensor and ε_{ij}^T denotes the total strain at a point. Based on homogenization theory for structurally inhomogeneous solids, we express $\varepsilon_{ij}^T(\mathbf{r})$ as the sum of spatially invariant homogeneous strain $\bar{\varepsilon}_{ij}$ and position-dependent heterogeneous strain field $\delta\varepsilon_{ij}(\mathbf{r})$ that vanishes when integrated over the total volume:

$$\varepsilon_{ij}^T(\mathbf{r}) = \bar{\varepsilon}_{ij} + \delta\varepsilon_{ij}(\mathbf{r}); \int_V \delta\varepsilon_{ij}(\mathbf{r})d^3\mathbf{r} = 0. \tag{10}$$

We use Khachaturyan's microelasticity theory with a homogeneous modulus approximation to solve the mechanical equilibrium equation [49]

$$\frac{\partial\sigma_{ij}}{\partial r_j} = C_{ijkl}\frac{\partial\left[\varepsilon_{kl}^T(\mathbf{r}) - Q_{klmn}P_m(\mathbf{r})P_n(\mathbf{r})\right]}{\partial r_j} = 0, \tag{11}$$

in Fourier space (assuming periodicity in local displacement and strain fields). In the absence of applied stress, homogeneous strain $\bar{\varepsilon}_{ij}$ is simply given by the weighted mean of total eigenstrain field:

$$\bar{\varepsilon}_{ij} = \sum_{p=0}^{5}\varepsilon_{ij}^p\Psi_p, \tag{12}$$

where $\Psi_p = (1/V)\int_V[\psi_p(\mathbf{r}) - \bar{\psi}_p]dV$ and $\psi_p(\mathbf{r}) = P_i(\mathbf{r})P_j(\mathbf{r})$ $(i, j = 1, 2, 3)$ and $p = 0, \ldots, 5$. Local displacement field in Fourier space, $\tilde{\mathbf{u}}(\mathbf{k})$, is obtained by solving Eq. (11)

$$\tilde{u}_k(\mathbf{k}) = -\mathrm{I}|\mathbf{k}|^{-1}n_j\Omega_{ik}(\mathbf{n})\sum_{p=0}^{5}\sigma_{ij}^p\Delta\tilde{\psi}_p(\mathbf{k}). \tag{13}$$

Here, $\mathbf{k}$ denotes the wave vector in the reciprocal space, $\mathbf{n} = \mathbf{k}/|\mathbf{k}|$, and $\mathrm{I} = \sqrt{-1}$. $\Omega_{ik}^{-1}(\mathbf{n}) = C_{ijkl}n_jn_l$ is the inverse of Green's function, ε_{ij}^p is the position-independent part of the eigenstrain tensor [Eq. (8)] associated with the field $\psi_p(\mathbf{r})$, and $\Delta\psi_p(\mathbf{r}) = \psi_p(\mathbf{r}) - \bar{\psi}_p$, and $\sigma_{ij}^p = C_{ijkl}\varepsilon_{kl}^p$. Using the displacement field from Eq. (13), we express the elastic energy in reciprocal space as follows:

$$\mathcal{F}_{\text{elastic}} = \frac{1}{2}\sum_{p,q=0}^{5}\int\frac{d^3\mathbf{k}}{(2\pi)^3}B_{pq}(\mathbf{n})\tilde{\psi}_p(\mathbf{k})\tilde{\psi}_q^*(\mathbf{k}), \tag{14}$$

where $B_{pq}(\mathbf{n}) = C_{ijkl}\varepsilon_{ij}^p\varepsilon_{kl}^q - n_i\sigma_{ij}^p\Omega_{jk}(\mathbf{n})\sigma_{kl}^qn_l$, and $\tilde{\psi}^*$ refers to the complex conjugate of $\tilde{\psi}$. A volume of $(2\pi)^3/V$ about $\mathbf{k} = 0$ is excluded from the integration in Eq. (14).

Assuming the domain wall energies to be isotropic, the gradient energy density f_{gradient} in Eq. (1) is written as

$$f_{\text{gradient}} = \tfrac{1}{2}G_{11}\left(P_{1,1}^2 + P_{1,2}^2 + P_{1,3}^2 + P_{2,1}^2 + P_{2,2}^2 + P_{2,3}^2 + P_{3,1}^2 + P_{3,2}^2 + P_{3,3}^2\right), \tag{15}$$

where $P_{i,j}$ denotes $\partial P_i/\partial x_j$. G_{11} is a positive gradient energy coefficient associated with the gradients in the polarization field. Although gradient energy coefficients generally form a fourth-rank tensor whose components can be determined using first-principles calculations [50,51] or can be fitted numerically and corresponding domain wall energies can be obtained by phase-field simulations [52], thus far no such calculation is reported for BZCT. Therefore we assume a scalar gradient energy coefficient in our model.

To include the effects of external fields in our thermodynamic stability analysis, we introduce external electromechanical fields in our model. For example, for a mechanically constrained (clamped) system that is not allowed to deform

along any direction ($\bar{\varepsilon}_{ij} = 0$), we introduce a uniform stress field $\bar{\sigma}_{ij}$ whose magnitude increases quadratically with polarization [36]:

$$\bar{\sigma}_{ij} = \frac{1}{V}\int_V C_{ijkl}\varepsilon^0_{kl}(\mathbf{r})dV = \frac{1}{V}\int_V C_{ijkl}Q_{klmn}P_m(\mathbf{r})P_n(\mathbf{r})dV = q_{ijmn}\langle P_m P_n\rangle. \tag{16}$$

Here, $\langle\cdot\rangle$ denotes the volume average of the quantity inside the angular brackets. When the macroscopic average stress $\bar{\sigma}_{ij}$ is zero everywhere in the system, we call it stress-free or unconstrained. To define a mechanically constrained state where the system is clamped in all directions, we set $\bar{\varepsilon}_{ij} = 0$. Considering bulk and elastic contributions to the total free energy density given in Eqs. (A1) and (9) [44], we construct the thermodynamic potential f^{cons} for mechanically constrained BZCT, given as

$$\begin{aligned} f^{\text{cons}} &= \tfrac{1}{2}\alpha_1\left(P_1^2+P_2^2+P_3^2\right) + \tfrac{1}{4}\alpha^e_{11}\left(P_1^4+P_2^4+P_3^4\right) \\ &+ \tfrac{1}{6}\alpha_{111}\left(P_1^6+P_2^6+P_3^6\right) + \tfrac{1}{2}\alpha^e_{12}\left(P_1^2P_2^2+P_2^2P_3^2+P_3^2P_1^2\right) \\ &+ \tfrac{1}{2}\alpha_{112}\left(P_1^4\left(P_2^2+P_3^2\right)+P_2^4\left(P_3^2+P_1^2\right)\right. \\ &\left.+ P_3^4\left(P_1^2+P_2^2\right)\right) + \tfrac{1}{6}\alpha_{123}P_1^2P_2^2P_3^2, \end{aligned} \tag{17}$$

where

$$\alpha^e_{11} = \alpha_{11} + 4\left\{\frac{1}{6}\left[\frac{\hat{q}^2_{11}}{\hat{C}_{11}} + 2\frac{\hat{q}^2_{22}}{\hat{C}_{22}}\right]\right\}, \tag{18a}$$

$$\alpha^e_{12} = \alpha_{12} + 2\left\{\frac{1}{6}\left[\frac{2\hat{q}^2_{11}}{\hat{C}_{11}} - 2\frac{\hat{q}^2_{22}}{\hat{C}_{22}} + 3\frac{q^2_{44}}{C_{44}}\right]\right\}, \tag{18b}$$

with

$$\begin{aligned} \hat{C}_{11} &= C_{11} + 2C_{12}, \\ \hat{C}_{22} &= C_{11} - C_{12}, \\ \hat{q}_{11} &= q_{11} + 2q_{12}, \\ \hat{q}_{22} &= q_{11} - q_{12}. \end{aligned} \tag{19}$$

Here, α^e_{11} and α^e_{12} are the modified Landau coefficient for a clamped system. The effective electrostrictive coefficients q_{ij} in Eq. (19) are defined as $q_{11} = C_{11}Q_{11} + 2C_{12}Q_{12}$, $q_{12} = C_{11}Q_{12} + C_{12}(Q_{11} + Q_{12})$, and $q_{44} = 2C_{44}Q_{44}$.

In Sec. III, we will use the comparison between coefficients α_{11}, α_{12} for the stress-free system and α^e_{11}, α^e_{12} for the constrained system to determine electrostrictive anisotropy effects on diffusionless phase diagrams and to examine changes in phase stability with the application of constraint. To compare polarization switching characteristics between stress-free and constrained BZCT, we include an additional term $\mathbf{P}\cdot\mathbf{E}_{\text{ext}}$ in Eqs. (A5) and (17) [53] to derive analytical expressions relating externally applied electric field $\mathbf{E}_{\text{ext}}$ to polarization and measure "theoretical" *P-E* loops analytically. Minimization of total energy with respect to polarization provides relations between external electric field and polarization for stress-free and constrained systems:

$$\begin{aligned} E^{\text{sf}}_{\text{ext}}(\phi) &= \frac{\partial f^{\text{sf}}_{\phi}}{\partial P}, \\ E^{\text{cons}}_{\text{ext}}(\phi) &= \frac{\partial f^{\text{cons}}_{\phi}}{\partial P}, \end{aligned} \tag{20}$$

where $\phi = T, O, R$. However, one should note that the analytically measured characteristics ignore spatial variations in the polarization field and the local interactions.

B. Phase-field model

To incorporate spatial interactions between the fields, we derive the following Euler-Lagrange equation for the polarization field $\mathbf{P}(\mathbf{r}, t)$ that minimizes the total free energy of the system [Eq. (1)] at a given temperature and composition:

$$\frac{\delta\mathcal{F}}{\delta P_i} = 0 \Rightarrow \frac{\partial f_{\text{bulk}}}{\partial P_i}\Big|_{P_i^{\text{eq}}} - E_i^{\text{eq}} + \sigma_{ij}^{\text{eq}}\frac{\partial\varepsilon^{\text{el}}_{ij}}{\partial P_i}\Big|_{P_i^{\text{eq}}} - G_{11}\frac{\partial^2 P_i}{\partial r_j^2}\Big|_{P_i^{\text{eq}}} = 0 \ (i = 1, 2, 3). \tag{21}$$

Here, E_i^{eq} and σ_{ij}^{eq} are obtained by solving electrostatic and mechanical equilibrium equations [Eqs. (6) and (11)]. The variational derivative $\delta\mathcal{F}/\delta P_i$ in Eq. (21) defines the driving force for domain evolution in the ferroelectric system.

Thus the Allen-Cahn equation governing spatiotemporal evolution of $\mathbf{P}(\mathbf{r}, t)$ is given as

$$\frac{\partial P_i(\mathbf{r}, t)}{\partial t} = -L\frac{\delta\mathcal{F}}{\delta P_i} \ (i = 1, 2, 3), \tag{22}$$

where L is a relaxation coefficient related to domain wall mobility in an overdamped system.

We solve Eq. (22) coupled with electrostatic and mechanical equilibrium equations [Eqs. (6) and (11)] in three-dimensions using a semi-implicit Fourier spectral method [54].

We use FFTW library along with OpenMP parallelization to numerically implement our phase-field model.

III. RESULTS AND DISCUSSION

In this section, we present the results of thermodynamic stability analysis of ferroelectric domains in BZCT system using the potential given in Eq. (A5). We also present the results of three-dimensional phase-field simulations of domain evolution in equimolar BZCT and the corresponding switching behavior as a function of applied electromechanical fields. We scale and nondimensionalize all parameters used in our study using characteristic values of length (L_c), energy (E_c), charge (q_c), and time (τ_c). Using the experimental values of spontaneous polarization $P_s = 0.2\,\text{C}/\text{m}^2$ and the reciprocal of dielectric susceptibility $|\alpha_1|_{\theta=298\text{K}} = 2.2781\times10^7\ \text{Jm}\,\text{C}^{-2}$ of equimolar BZCT at room temperature (298 K), we obtain $E_c = 4.1\times10^{-21}$ J, $L_c = 1.65$ nm [55], and $q_c = P_s(L_c^2) = 5.445\times10^{-19}$ C. We use the factor $|\alpha_1|_{\theta=298\text{K}}P_s^2 = 9.11\times10^5\ \text{J}\,\text{m}^{-3}$ to normalize all parameters appearing in the governing equations [Eqs. (6), (11), and (22)]. The characteristic time τ_c is determined using the relation $|\alpha_1|_{\theta=298\text{K}}L\tau_c = 1$, where L denotes the dimensional value of relaxation coefficient. The dimensional gradient energy coefficient G_{110} is given as $G_{110} = L_c^2|\alpha_1|_{\theta=298\text{K}} = 6.2\times10^{-11}\ \text{J}\,\text{m}^3/\text{C}^2$ corresponding to a nondimensional value $G'_{110} = 1$. Phase-field simulations are carried out in a $200\Delta\times200\Delta\times200\Delta$ simulation box where $\Delta = 0.32$ nm is the grid spacing (corresponding to a nondimensional spacing $\Delta' = 1$). We choose a nondimensional time step $\Delta t' = 0.01$ to ensure

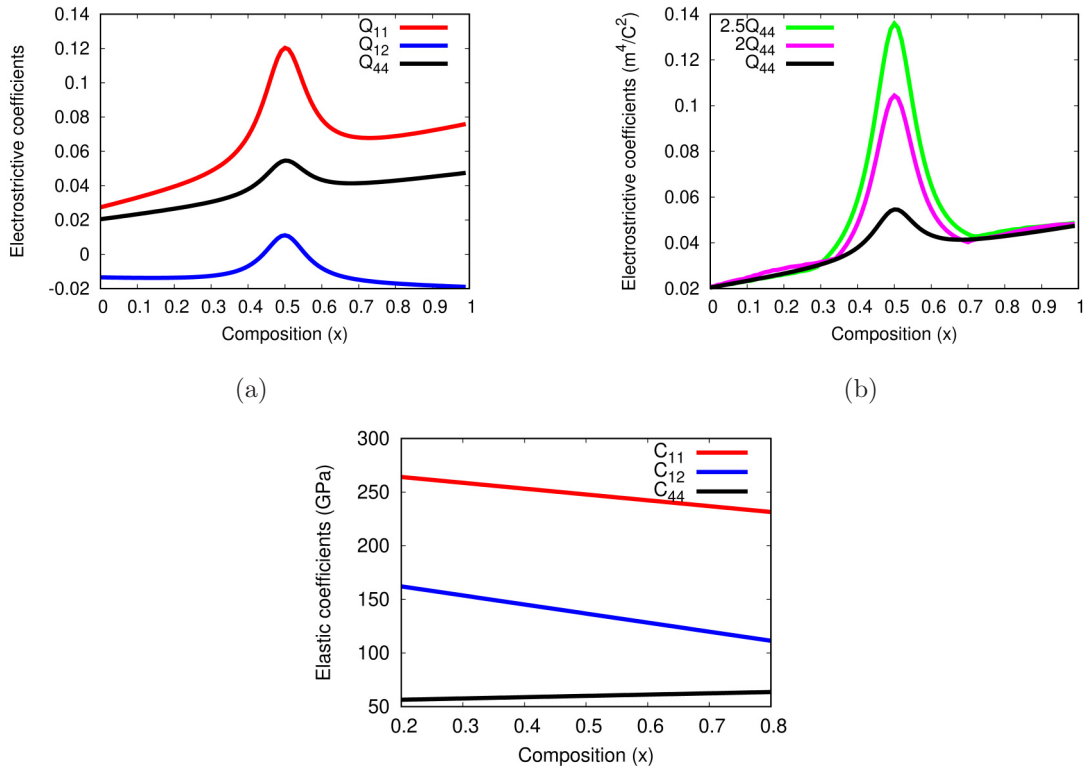

FIG. 1. (a) Variation of Q_{11}, Q_{12}, Q_{44} with composition x when $Q_z = 1$. (b) Change in $Q_z = \frac{2Q_{44}}{Q_{11}-Q_{12}}$ is realized through the change in Q_{44} keeping Q_{11} and Q_{12} unchanged: (case 1) $Q_z = 1$, $Q_{44} = Q_{44}$, (case 2) $Q_z = 2$, $Q_{44} = 2Q_{44}$, and (case 3) $Q_z = 2.5$, $Q_{44} = 2.5Q_{44}$. (c) Variation of elastic moduli C_{11} and C_{12} as a function of composition x.

high spatiotemporal accuracy. Since our model uses spontaneous polarization as the order parameter field, we specify a nondimensional background dielectric constant $\epsilon_b = 8$ to describe dielectric screening effects of high frequency polar phonon modes (e.g., electronic polarization) [56]. Moreover, we assume the elastic and electrostrictive coefficients (C_{ij} and Q_{ij} $i, j = 1, \ldots, 6$) to be invariant with temperature θ as long as θ does not exceed the Curie temperature $\theta_c(x)$ for a given composition x. Due to limited experimental data across entire composition range of BZCT system, we have assumed the functional forms of composition dependency of these coefficients to be similar to those used in PZT. Using experimental values of piezoelectric voltage constants and elastic moduli for the terminal and equimolar compositions ($x = 0, 1, 0.5$) of BZCT as fitting parameters [57], we arrive at the following relations for $C_{ij}(x)$ and $Q_{ij}(x)$:

$$\begin{aligned}
C_{ij}(x) &= xC_{ij}^{\mathrm{BZT}} + (1-x)C_{ijkl}^{\mathrm{BCT}},\\
Q_{11}(x) &= 0.04895x + 0.02605\\
&\quad + 0.069778/(1 + 200(x-0.5)^2),\\
Q_{12}(x) &= -0.0056x - 0.01400\\
&\quad + 0.0279/(1 + 200(x-0.5)^2),\\
Q_{44}(x) &= 0.02728x + 0.02002\\
&\quad + 0.02095/(1 + 200(x-0.5)^2). \qquad (23)
\end{aligned}$$

Figure 1 shows the variation of Q_{ij} and C_{ij} with composition. Although the elastic moduli C_{ij} vary linearly with composition, the electrostrictive coefficients Q_{11}, Q_{12} and Q_{44} show a pronounced maximum at $x = 0.5$. Following Yang *et al.* [42], we express the composition and temperature dependent Landau free energy coefficients as follows:

$$\begin{aligned}
\alpha_1(\theta, x) &= \alpha_0(\theta - \theta_c(x)),\\
\beta_1(\theta, x) &= \beta_{11}(x - x_{\mathrm{quad}}) + \beta_{12}(\theta - \theta_{\mathrm{quad}}),\\
\gamma_1(\theta, x) &= \gamma_{11} + \gamma_{12}(x - x_{\mathrm{quad}}),\\
\beta_2(\theta, x) &= \beta_{21}(x - x_{\mathrm{quad}}) + \beta_{22}(\theta - \theta_{\mathrm{quad}}),\\
\gamma_2(\theta, x) &= \gamma_{21}(x - x_{\mathrm{quad}}),\\
\gamma_3(\theta, x) &= \gamma_{31}(x - x_{\mathrm{quad}}) + \gamma_{32}(\theta - \theta_{\mathrm{quad}}), \qquad (24)
\end{aligned}$$

where $\alpha_0 = 4.142 \times 10^5$, $\beta_{11} = -1.2 \times 10^8$, $\beta_{12} = 7.56 \times 10^5$, $\gamma_{11} = 7.764 \times 10^8$, $\gamma_{12} = 4 \times 10^7$, $\beta_{21} = -1.2 \times 10^8$, $\beta_{22} = -7.56 \times 10^5$, $\gamma_{21} = -2.2 \times 10^8$, $\gamma_{31} = 1.0 \times 10^{11}$, $\gamma_{32} = 2.1 \times 10^8$ are the values in SI units, $\alpha_0 = 1/(\epsilon_0 C_0)$, $\epsilon_0 = 8.854 \times 10^{-12}$ $\mathrm{C^2\,N^{-1}\,m^{-2}}$ is the permittivity of free space, C_0 is the average Curie constant, θ denotes the temperature in Kelvin, x denotes the composition of BZT (in mole fraction), $\theta_c(x) = \theta_C^{\mathrm{BZT}} + (\theta_C^{\mathrm{BCT}} - \theta_C^{\mathrm{BZT}})x$ is the composition-dependent Curie temperature of the BZCT system, where θ_C^{BZT} is the Curie temperature of pure BZT ($x = 0$), θ_C^{BCT} is the Curie temperature of BCT ($x = 1$), θ_{quad} and x_{quad} denote the temperature and the composition

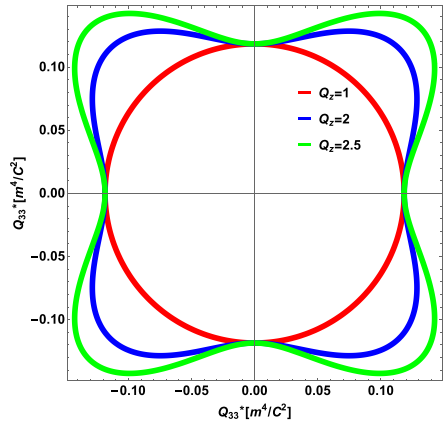

(a) Two dimensional representation of the orientation dependence of electrostrictive coefficient Q_{33}^* for BZCT system.

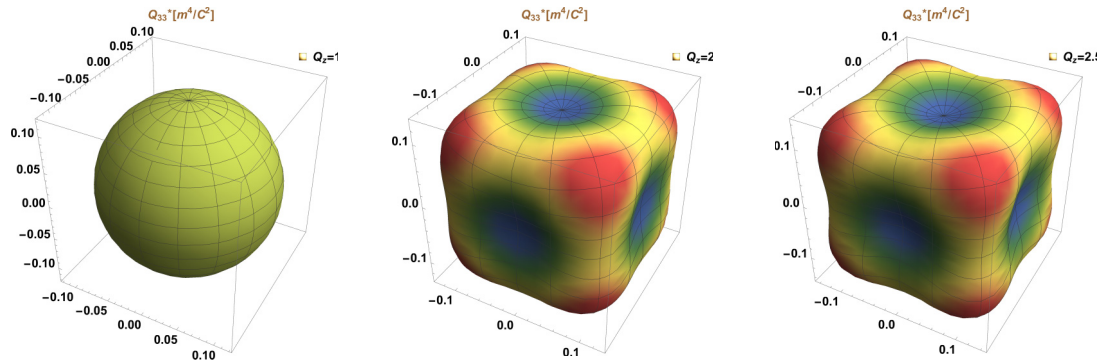

(b) Case 1 (c) Case 2 (d) Case 3

FIG. 2. The orientation dependence of electrostrictive coefficient Q_{33}^* for BZCT system for three different cases.

at the quadruple point defined by the coexistence of the paraelectric cubic phase and ferroelectric T, O and R phases in BZCT. The Landau coefficients are obtained by fitting the experimental values of $\theta_{\text{quad}} = 335$ K, $x_{\text{quad}} = 0.35$, $\theta_c^{\text{BZT}} = 293$ K, $\theta_c^{\text{BCT}} = 393$ K. and equilibrium spontaneous polarization $P_{s,\phi}$ $\phi = T, O, R$ of the polar phases measured at room temperature.

The values of all the Landau coefficients are obtained from the above-mentioned form using the relations showed in Table III in Appendix A. Both dimensional and nondimensional forms of all coefficients used in our study are tabulated in Ref. [58]. Here, all parameters are normalized using $|\alpha_1|_{\theta=298\,\text{K}} P_0^2$ J m^{-3}, where $P_0 = 0.2$ C m^{-2} is the experimentally determined spontaneous polarization of BCZT at $x = 0.5$, $\theta = 298$ K, and the nondimensional temperature $\theta' = \theta/298$.

Several experimental studies have found a strong correlation between dielectric and piezoelectric anisotropy and attributed this to the intrinsic anisotropy in electrostrictive coefficients stemming from the change in structure of BO_6 oxygen octahedra in perovskite [29,33,34]. Thus, when processing conditions (involving change in chemistry and application of external electromechanical fields) trigger a change in the geometry of oxygen octahedra of the ferroelectric perovskite (manifested by change in tilt angle of BO_6 octahedra), there is a subsequent change in the inherent anisotropy associated with electrostrictive coefficients [59,60]. To understand the role of electromechanical anisotropy on the stability of ferroelectric domains and consequent switching dynamics, we define an electrostrictive anisotropy parameter $Q_z = \frac{2Q_{44}}{Q_{11}-Q_{12}}$ and systematically investigate the role of Q_z on switching behavior of BZCT. Studies also report another measure of electrostrictive anisotropy $Q_a = \frac{Q_{11}-Q_{12}}{Q_{44}}$ [29]. Our definition of Q_z is in the same spirit as the Zener anisotropy parameter A_Z associated with elastic stiffness tensor that distinguishes between elastically soft and hard directions in orthotropic materials [31]. Moreover, one should note that electrostrictive anisotropy and anisotropy in spontaneous strain is related because the spatially invariant part of spontaneous strain (eigenstrain ε^0) is solely a function of electrostrictive coefficients Q [see Eq. (8)].

To demonstrate the correlations between electrostrictive anisotropy and domain stability/switching in BZCT, we choose three cases based on the value of Q_z:

(case 1) $Q_z = 1$ ($Q_a = 2$),
(case 2) $Q_z = 2$ ($Q_a = 1$),
(case 3) $Q_z = 2.5$ ($Q_a = 0.8$).
We define an electrostrictive modulus Q^*_{33} as follows:

$$\frac{1}{Q^*_{33}} = \frac{Q_{11}+Q_{12}}{(Q_{11}-Q_{12})(Q_{11}+2Q_{12})} - \frac{2(Q_z-1)}{Q_z(Q_{11}-Q_{12})}\left(l_1^2 l_2^2 + l_2^2 l_3^2 + l_1^2 l_3^2\right), \tag{25}$$

to show the orientation dependence of fourth-order electrostrictive tensor in two and three dimensions (Fig. 2) and l_k represent the direction cosines of the moduli with respect to the three positive coordinate axes [32].

When $Q_z = 1$ (case 1), the representation quadric is spherical indicating isotropic behavior, whereas when $Q_z > 1$ (cases 2 and 3), the surfaces become anisotropic showing lower values of Q^*_{33} along ⟨100⟩ directions (Fig. 2). Note that $Q_z > 1$ introduces anisotropy in electrostriction in the paraelectric state. Thus we need to use Eq. (8) to determine the spontaneous strain components of the ferroelectric phases and define elastic energy according to Eq. (14) for a given Q_z. Since all ferroelectric variants are also ferroelastic, preferred orientations of variants are determined by the minimization of elastic interactions between the variants. However, one should note that the stable domain configuration in a stress-free, electrically neutral ferroelectric system requires minimization of total energy arising from coupled elastic and electric interactions.

A. Diffusionless phase diagram

Minimization of $f^{\text{modified}}_{\text{bulk}}$ in Eq. (A5) determines the polarization states of the stable phases in electrically neutral, stress-free BZCT at any given temperature θ and composition x. Phase-coexistence conditions are derived as follows. When O alone is the stable phase, phase stability condition using Eq (A6) leads to an inequality

$$\frac{\beta_2}{\gamma_2 P^2_{\text{eq}}} > -1. \tag{26}$$

This implies that $|\beta_2| > \gamma_2 P^2_{\text{eq}}$. However, when two phases coexist (e.g., T and O), the stability condition becomes an equality given as

$$\frac{1}{2}\beta_2 P^4_{\text{eq}} = -\frac{1}{12}\gamma_2 P^6_{\text{eq}}, \tag{27}$$

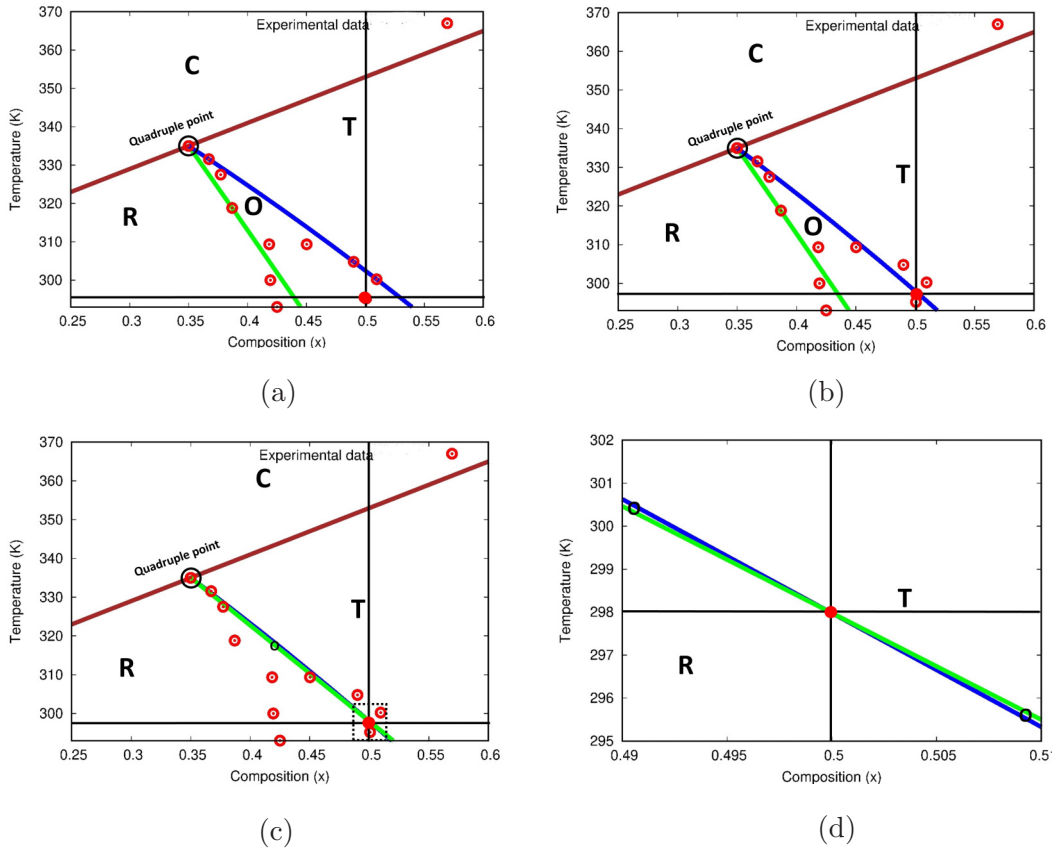

FIG. 3. Computed diffusionless phase diagrams of BZCT system as a function of electrostrictive anisotropy parameter Q_z and their comparison with experimental data. Experimental data for comparison are obtained from [25,37,61]. Here, C, T, O, and R denote cubic, tetragonal, orthorhombic and rhombohedral phases, respectively. The black solid line and the red dot in each diagram correspond to the equimolar composition of BZCT at room temperature ($x = 0.5$, $T = 298$ K). Note that in cases 2 and 3, the predictions of phase stability at the equimolar composition $x = 0.5$ at ambient temperature and pressure ($T = 298$ K, $P = 1$ atm.) agree with the experimental observations [26,27]. (a) Case 1. (b) Case 2. (c) Case 3. (d) Zoomed image of the marked portion for case 3.

TABLE I. Values of β_2 for different Q_z.

Q_z	Form of β_2
1	$-1.2\times10^8(x-x_{\text{quad}})+-7.56\times10^5(\theta-\theta_{\text{quad}})$
2	$-1.4198\times10^8(x-x_{\text{quad}})+-7.56\times10^5(\theta-\theta_{\text{quad}})$
2.5	$-1.02846\times10^8(x-x_{\text{quad}})+-7.56\times10^5(\theta-\theta_{\text{quad}})$

implying $|\beta_2| = \gamma_2 P_{\text{eq}}^2$. Similarly, phase stability conditions for a three-phase coexistence (i.e., a stable phase mixture of T, R, and O) is given as

$$\frac{1}{2}\beta_2 P_{\text{eq}}^4 = -\frac{1}{12}\gamma_2 P_{\text{eq}}^6 = \frac{1}{36}\gamma_3 P_{\text{eq}}^6. \tag{28}$$

For a given temperature and any composition lying within the MPR, we may assume either γ_2 or γ_3 to be a constant. Assuming a fixed value of γ_2 at a given temperature and composition and requiring γ_2 to be positive to ensure a first order transition, we find the absolute value of β_2 to decrease with a corresponding increase in the number of degenerate minima of Landau free energy corresponding to coexistence of polar phases. Since $|\beta_2|$ is a measure of the extent of polar anisotropy of the free energy, our analysis confirms reduction in polar anisotropy when more polar phases coexist (i.e., the free energies of the polar phases become degenerate). Moreover, we note that $\beta_1 = \alpha_{12}$ remains unchanged and does not contribute to the polar anisotropy.

We equate the anisotropic contributions to the free energy of each phase [Eq. (A6)] to calculate the temperature-composition ($\theta - x$) relations for the "T-O" and "O-R" phase boundaries [37]. These are given as follows:

$$\theta_{OT} = \theta_{\text{quad}} - \frac{1}{\beta_{22}}\left[\beta_{21} + \gamma_{21}P_{\text{eq}}^2\right](x - x_{\text{quad}}), \tag{29}$$

$$\theta_{OR} = \theta_{\text{quad}} - \frac{1}{\beta_{22} - \frac{4}{27}\gamma_{32}P_{\text{eq}}^2}\left[\beta_{21} + \left(\frac{5}{9}\gamma_{21} - \frac{4}{27}\gamma_{31}\right)P_{\text{eq}}^2\right] (x - x_{\text{quad}}), \tag{30}$$

where the equilibrium polarization P_{eq} values at the T-O and O-R phase boundaries are obtained by assuming a weak first order transition along phase-coexistence lines. Thus $P_{\text{eq}}^{T-O} = P_{\text{eq},T}$ or $P_{\text{eq},O}$, and $P_{\text{eq}}^{O-R} = P_{\text{eq},O}$ or $P_{\text{eq},R}$, where the equilibrium values of polarization are given in Eq. (A7).

To determine the interrelation between Q_z and the Landau free energy coefficients α_{ij}, we proceed as follows: first, we find $\beta_2 = \alpha_{11} - \alpha_{12}$ from the phase-coexistence conditions [Eqs. (26)–(28)] keeping $\beta_1 = \alpha_{12}$ fixed. Next, for $Q_z = 1$, we find relations between stress-free α_{11}, α_{12} and constrained α_{11}^e, α_{12}^e from Eq. (18). Demanding the difference in the constrained coefficients, $\alpha_{11}^e - \alpha_{12}^e$ or β_2^e, and the unconstrained coefficient α_{12} to be invariant for all Q_z, we find the change in

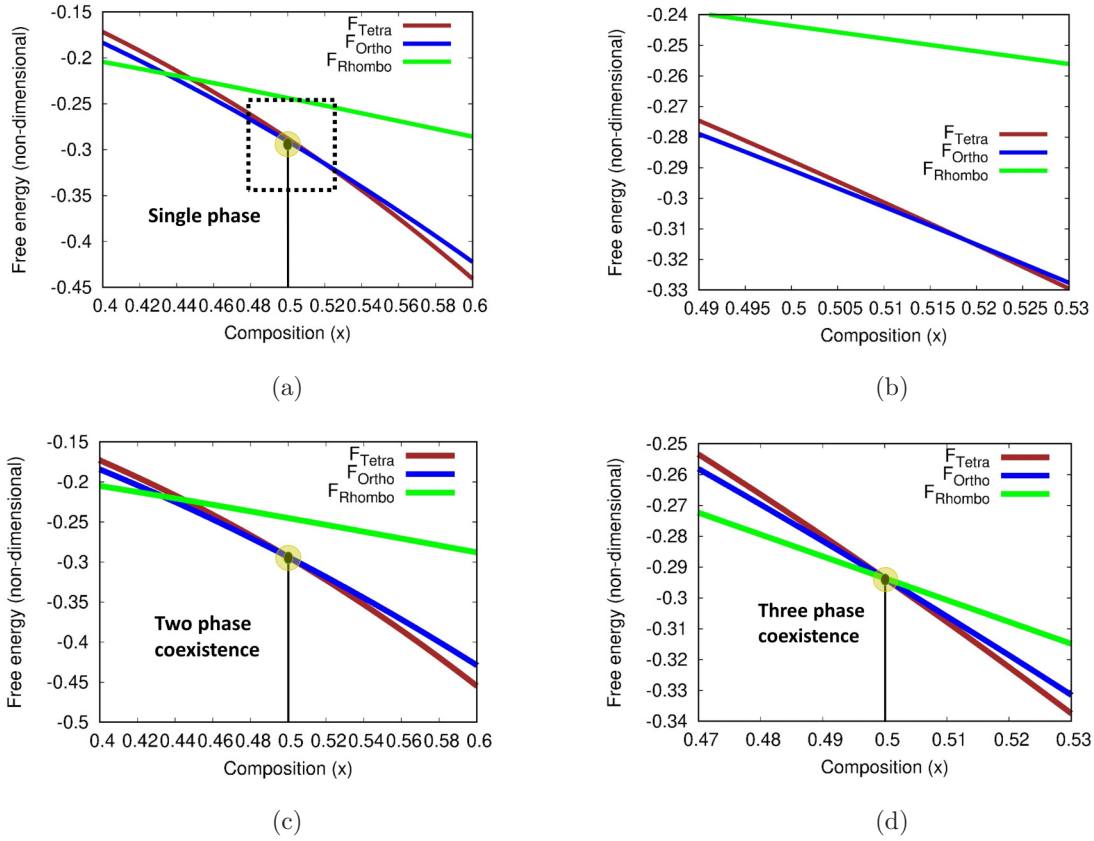

FIG. 4. Free energy composition diagrams for different cases of electrostrictive anisotropy: [(a) and (b)] case 1 with a zoomed region around the equimolar composition indicating lowest energy for the orthorhombic phase at $x = 0.5$, (c) case 2 showing $T + O$ coexistence, (d) case 3 showing $T + R + O$ coexistence.

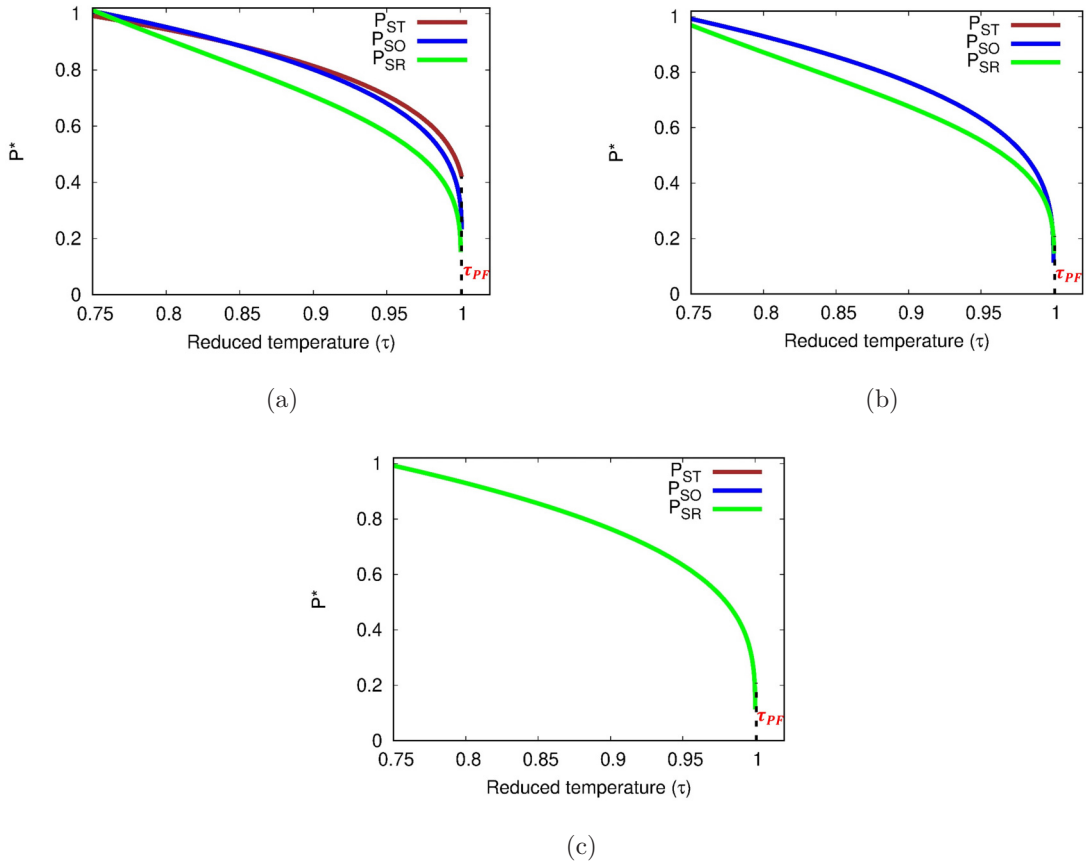

FIG. 5. Computed spontaneous polarization of ferroelectric phases T, R as a function of temperature at $x = 0.5$ for BZCT solid solution for the three different cases. (a) Computed spontaneous polarization for all the phases for case 1. (b) Computed spontaneous polarization for all the phases for case 2. (c) Computed spontaneous polarization for all the phases case 3.

Q_{44} as a function of α_{11}:

$$Q_{44} = \left[\frac{1}{4C_{44}}\left\{(\alpha_{11} - \alpha_{12}) - \left(\alpha^e_{11} - \alpha^e_{12}\right) + 2\frac{\hat{q}^2_{22}}{\hat{C}_{22}}\right\}\right]^{\frac{1}{2}} \text{or}$$

$$Q_{44} = \left[\frac{1}{4C_{44}}\left\{\beta_2 - \beta^e_2 + 2\frac{\hat{q}^2_{22}}{\hat{C}_{22}}\right\}\right]^{\frac{1}{2}}. \quad (31)$$

When Q_z is greater than unity, α_{11} decreases with increasing Q_z.

In Fig. 3, we present the computed temperature-composition phase diagrams for different values of β_2. The forms of β_2 for different Q_z are defined in Table I. For case 1 ($Q_z = 1$), the shapes of the computed T-O and O-R MPBs show good agreement with experimental data obtained from high resolution x-ray diffraction studies [25], and the MPR contains only O phase. When Q_z becomes anisotropic, thermodynamic stability within the MPR changes from single phase O to a mixture of T and O phases for case 2 [$Q_z = 2$, Fig. 3(b)] and a mixture of all three polar phases $T + R + O$ in case 3 [$Q_z = 2.5$, Fig. 3(c)]. Figure 3(d) displays the zoomed version of the region marked in Fig. 3(c) also shows the coexistence of all the three phases ($T + R + O$) at the equimolar composition. Thus it is evident from the computed diagrams that the increase in electrostrictive anisotropy leads to a reduction in the polar anisotropic contribution to the free energy.

Having established the correspondence between β_2, α_{11}, and Q_z, we plot the free energies of T, O, and R phases as a function of x at room temperature for all cases (Fig. 4). We are particularly interested in examining phase stability at $x = 0.5$ where most of the experimental reports are available [25–27,37,61]. When $Q_z = 1$, the O phase has lowest free energy among all the polar phases of BZCT. As Q_z increases, there is a reduction in the free energy of T and R. Thus, when $Q_z = 2$, we find the energies of T and O to be equal at $x = 0.5$. With a further increase in Q_z to 2.5, we get equal free energies for T, O, and R at $x = 0.5$. Although the overall energy of the system at $x = 0.5$ shows minimal variation with the change in Q_z, energies of T and R phases decrease with increasing Q_z such that T-O intersection ($f_T = f_O$) moves towards decreasing x while the O-R intersection ($f_O = f_R$) moves in the opposite direction. Brajesh *et al.* [26,27] showed a change in the phase stability of BZCT from three-phase ($T + O + R$) to two-phase ($T + O$) when it is subjected to a stress-relief anneal at 400 °C far above θ_c. They attributed this change to a stress-induced phase transformation occurring at 400 °C. Change in the anisotropy of electrostrictive coefficients of the paraelectric phase correspond to such stress-induced transformations preceding paraelectric → ferroelectric transition. Since the spatially invariant part of the spontaneous strain tensor is a function of electrostrictive coefficients for any given x [Eq. (8)], a change in Q_z alters the spontaneous

strain tensors associated with the ferroelectric phases thereby affecting phase stability. Figure 5 shows the variation of scaled spontaneous polarization $P^* = P/P_s$ of T, O and R phases of equimolar as a function of reduced temperature $\tau = \theta/\theta_c$ [Eq. (A7)]. When $Q_z = 1$, the stable O has the highest value of spontaneous polarization at room temperature ($\theta = 298$ K, $\tau = 0.84$). On the other hand, for $Q_z = 2$, T and O phases have the same P^* at room temperature which is greater than the spontaneous polarization of R. While, for $Q_z = 2.5$, T, R, and O have the same P^* at all temperatures up to $\theta = \theta_c$. This corroborates our observation of degeneracy of free energies of the ferroelectric phases with increasing Q_z at the equimolar morphotropic composition $x = 0.5$. The corresponding components of spontaneous strain tensor for each polar phase can be calculated using Eq. (8). Thus two independent components of spontaneous strain associated with T phase are $\varepsilon_1^0 = Q_{11}P_{s,T}^2$, $\varepsilon_2^0 = \varepsilon_3^0 = Q_{12}P_{s,T}^2$. The O phase possesses three independent components: $\varepsilon_1^0 = \varepsilon_2^0 = \frac{1}{2}(Q_{11} + Q_{12})P_{s,O}^2$, $\varepsilon_3^0 = Q_{12}P_{s,O}^2$, $\varepsilon_6^0 = \frac{1}{2}Q_{44}P_{s,O}^2$, and the R phase possesses two independent components: $\varepsilon_1^0 = \varepsilon_2^0 = \varepsilon_3^0 = \frac{1}{3}(Q_{11} + Q_{12})P_{s,R}^2$, $\varepsilon_4^0 = \varepsilon_5^0 = \varepsilon_6^0 = \frac{1}{3}Q_{44}P_{s,R}^2$. Here, $P_{s,T}$, $P_{s,O}$, and $P_{s,R}$, given in Eqs. (A7a), (A7b), and (A7c), represent the spontaneous polarization of T, O, and R phases, respectively.

B. Morphological evolution of domains

Figure 6 shows the evolution of ferroelectric domains to a steady state in equimolar BZCT at room temperature for all three cases of Q_z in the absence of external electromechanical fields. Thus, in all cases, the system is assumed to be stress-free with periodic boundary conditions on polarization (**P**), displacement (**u**), and electric potential (ϕ) fields. Note that for bulk ferroelectric systems the contribution to depolarization energy due to surface bound charge is zero (i.e., electrically unbounded domain: $\mathbf{E} \to \mathbf{0}$ as $\mathbf{r} \to \infty$). In all cases we start with the same random initial configuration which allows nucleation of any of the ferroelectric phases below θ_c.

When $Q_z = 1$, evolution leads to the formation of multiple variants of O phase [Fig. 7(a)]. The domain walls of these variants show specific crystallographic orientation. Analysis of mechanical compatibility using the difference in spontaneous strain between neighboring variants point to ferroelastic nature of the 60° and 120° domain walls. Even the 180° domain walls (O_3^+/O_3^-) show specific crystallographic orientation. The steady state domain structure consists of a regular twin-related arrangement of plate shaped O domains separated by straight domain walls. Such a strain accommodating arrangement of plates leads to reduction in elastic energy of the configuration. Absence of curvature of the domain walls indicates stress-free nature of the domains and local electroneutrality at the domain walls. The trijunctions and quadrijunctions formed by the intersection of 60°/120°/180° domain walls are regions with increased electrostatic and elastic interactions [Figs. 7(d) and 7(g)].

When $Q_z = 2$ (case 2), evolution at early stages leads to formation of discrete islands of T (T_3^+/T_3^-) in O (O_6^-) matrix [Fig. 6(b)]. These islands eventually get connected and arrange in the form of thin striped network dividing the continuous O domain into discrete parallel plates. Thus the steady state configuration shows a parallel plate geometry with the stripes of T dividing the O_6^- domain into discrete plates [Fig. 7(b)]. Although the straight walls separating the plates of $T + O$ are associated with low strain and electric energy, there is a marked increase in electrostatic and elastic interactions when T_3^+/T_3^- 180° domain walls intersect with O_6^- domains leading to an increase in curvature of T/O boundaries around the junction [Figs. 7(e) and 7(h)].

In case 3, evolution starts with clusters of all the three polar phases, T, R, and O, distributed homogeneously throughout the volume [Fig. 6(c)]. Growth of these clusters leads to a steady state twinned pattern wherein the plates of T, R, O variants wedge into one another forming nearly equal number of T-R, R-O, and T-O boundaries [Fig. 7(c)]. The domain

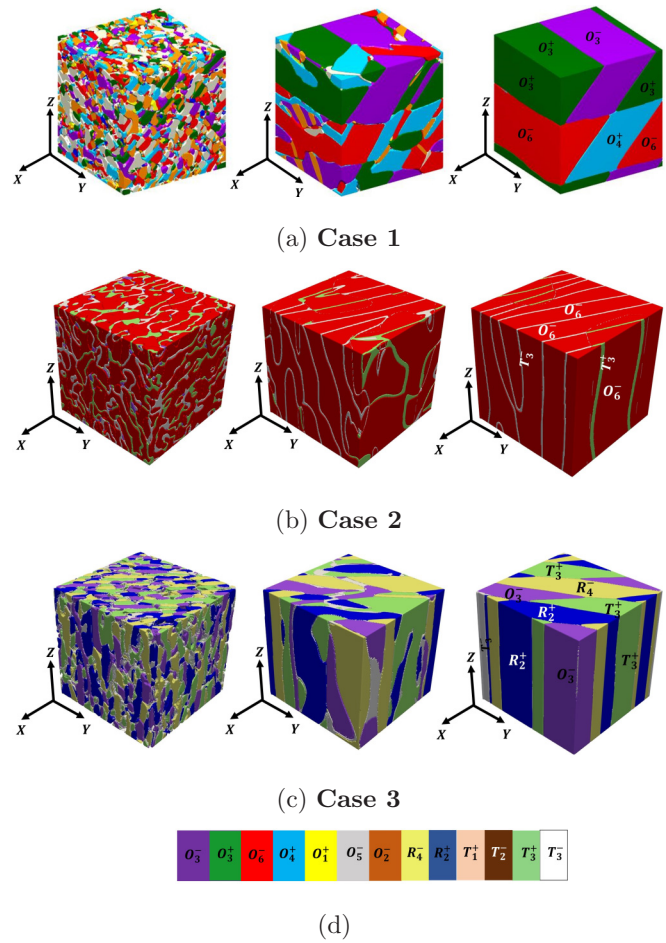

FIG. 6. Evolution of domain structures of equimolar BZCT at room temperature for three cases of electrostrictive anisotropy: (a) case 1 ($Q_z = 1$), (b) case 2 ($Q_z = 2$), and (c) case 3 ($Q_z = 2.5$). In all cases, time snapshots of evolution are shown at nondimensional times $t = 10\,000$, $50\,000$, and $150\,000$ (steady state configuration). The colors distinguish between variants of T, R, and O. (d) List of distinct colors corresponding to each variant. Components of polarization vector corresponding to each variant are given below: $O_1^+ : [110]$, $O_1^- : [\bar{1}\bar{1}0]$, $O_2^+ : [011]$, $O_2^- : [0\bar{1}\bar{1}]$, $O_3^+ : [101]$, $O_3^- : [\bar{1}0\bar{1}]$, $O_4^+ : [1\bar{1}0]$, $O_4^- : [\bar{1}10]$, $O_5^+ : [0\bar{1}1]$, $O_5^- : [01\bar{1}]$, $O_6^+ : [\bar{1}01]$, $O_6^- : [10\bar{1}]$, $T_3^+ : [001]$, $T_3^- : [00\bar{1}]$, $R_2^+ : [1\bar{1}\bar{1}]$, $R_4^- : [1\bar{1}1]$.

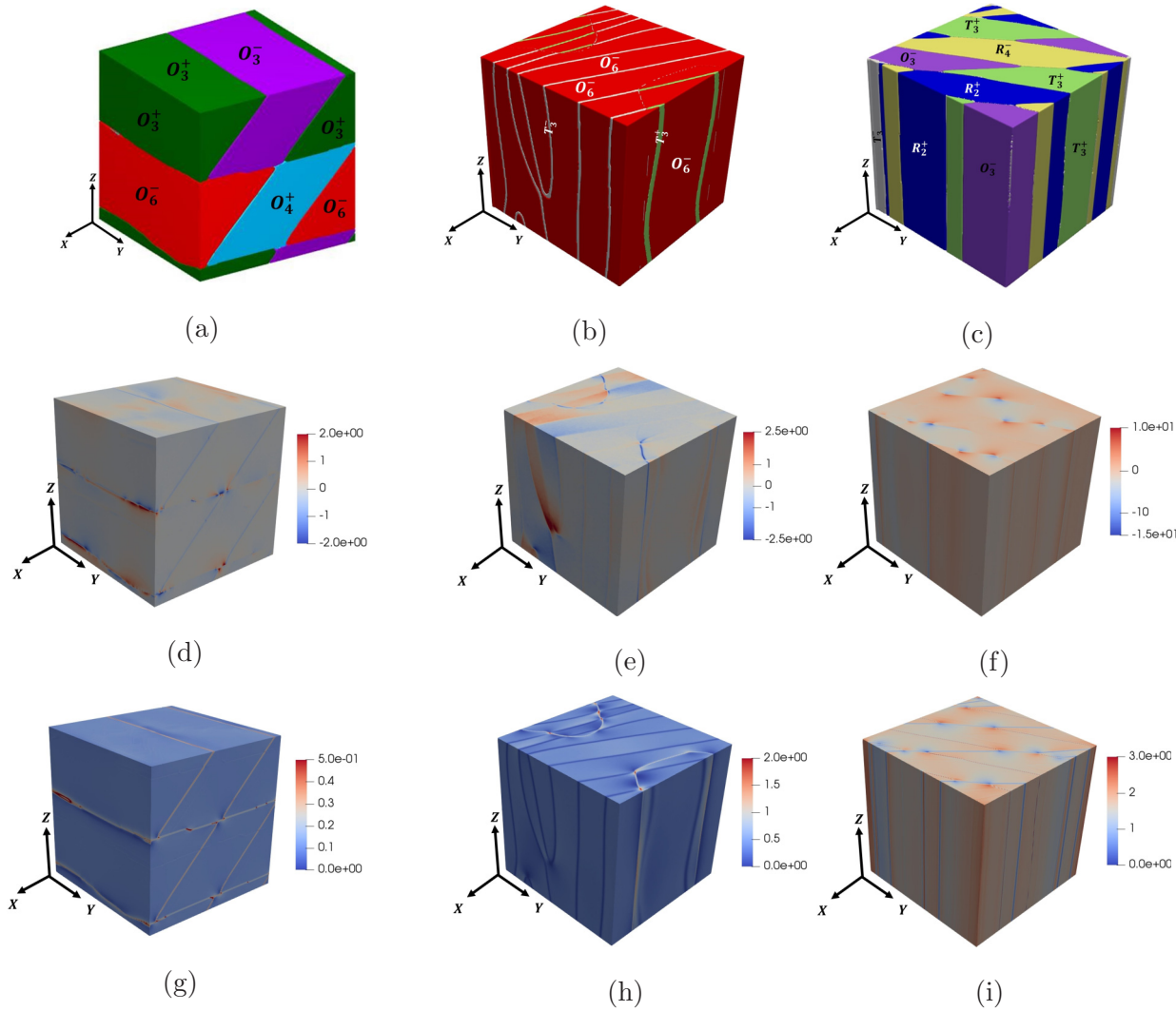

FIG. 7. Simulated microstructures at room temperature showing steady state spatial distribution of polar domains in stress-free equimolar BZCT as a function of electrostrictive anisotropy: (a) case 1: single phase orthorhombic, (b) case 2: coexistence of T and O domains, and (c) case 3: coexistence of T, R, and O domains. [(d)–(f)] Electric energy distribution (nondimensional) corresponding to cases 1, 2, and 3, respectively; [(g)–(i)] corresponding nondimensional elastic energy distribution. Energy distribution [(g)–(i)] $O_1^+ : [110]$, $O_1^- : [\bar{1}\bar{1}0]$, $O_2^+ : [011]$, $O_2^- : [0\bar{1}\bar{1}]$, $O_3^+ : [101]$, $O_3^- : [\bar{1}0\bar{1}]$, $O_4^+ : [1\bar{1}0]$, $O_4^- : [\bar{1}10]$, $O_5^+ : [0\bar{1}1]$, $O_5^- : [01\bar{1}]$, $O_6^+ : [\bar{1}01]$, $O_6^- : [10\bar{1}]$, $T_3^+ : [001]$, $T_3^- : [00\bar{1}]$, $R_2^+ : [\bar{1}11]$, $R_4^- : [\bar{1}\bar{1}\bar{1}]$.

pattern has the lowest average value of electric energy among these cases. However, at the triple junctions formed by the wedges of T, R, and O, we see an increase in electrostatic and elastic interactions [Figs. 7(f) and 7(i)]. Moreover, in all the cases, increase in elastic energy at the domain walls leads to a reduction in electric energy and vice versa indicating dual ferroelectric-ferroelastic character of these walls.

The domain walls display a common feature—they show a regular step-terrace structure where the steps are nearly perpendicular to domain wall orientations (Fig. 8), although step sizes vary for different combinations of orientation. Such a step-terrace structure suggests multistep switching via successive ferroelastic steps instead of single-step 180° switching [62].

Figure 9 shows the formation of the step-terrace morphology at the O_4^+ and O_6^- domain boundaries. The vector plot in Fig. 9(b) describes the step—terrace structure of the corresponding O_4^+ and O_6^- in Fig. 9(a).

We can understand the concept of the step-terrace morphology in view of the presence of surface bound charge at the domain wall. The expression for the surface bound charge can be written as $\sigma_P = (\mathbf{P_2} - \mathbf{P_1}) \cdot \hat{\mathbf{s}}$. Here $\hat{\mathbf{s}}$ is the unit vector normal to the domain wall. The domain walls associated with the nonzero bound charge are termed as charged domain walls. Since the presence of bound charge creates local electrostatic fields inside the domains, which is energetically costly, the head → head as well as tail → tail configurations lead to charged domain walls with higher electrostatic energy. The domain walls that do not carry any bound charge ($\sigma_P = 0$) is termed as the electroneutral domain walls.

For investigation and visualization of the step-terrace morphology we consider a system consisting of two domains

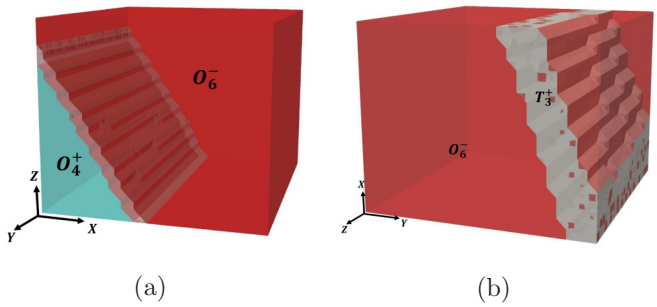

(a) (b)

FIG. 8. Domain wall configurations showing the step-terrace morphology from our phase-field simulations: (a) *O*-*O* and (b) *T*-*O* domain wall.

$O_4^+[1\bar{1}0]$ (marked as blue) and $O_6^-[10\bar{1}]$ (marked as red) represented by the planner view in Fig. 10(a). As the system evolves the domains reorient themselves leading to the formation of the step-terrace structure to maintain the proper head → tail configuration [Figs. 10(a)–10(e)]. The zoomed version of the final domain configuration [Fig. 10(f)] provide a guide to the eye of the pathway of the step-terrace structure.

Note that the alignment of the domains in the particular ways can introduce anisotropy, thus indicating the structural stability is driven by the Q_z anisotropy. Change in Q_z can change the easy polarization directions in ferroelectric system (measured by the ease of switching under an applied field) leading to variations in switching characteristics. To quantify such a variation we measure the difference between effective d_{31} and d_{33} as a function of Q_z. Therefore, in each case, we subject the steady state domain structure (obtained at zero electric field) to an applied field varying between −450 and 450 kV cm^{-1} with a step size of ±5 kV cm^{-1} along [001] (E_3) and [100] (E_1) directions to compute the electromechanical switching properties given by polarization hysteresis loop ($\bar{P}_z - E_3$), longitudinal strain hysteresis loop ($\epsilon_{33} - E_3$) and transverse strain hysteresis loop ($\epsilon_{33} - E_1$). The computed $\epsilon_{33} - E_3$ and $\epsilon_{33} - E_1$ [Figs. 11(b) and 11(d)] loops for all cases show a typical butterfly shape that is symmetric about zero applied field. We use the longitudinal and transverse strain hysteresis loops to determine the coercive field E_{coer} (defined as the field required for complete reversal of polarization) along [001] and [100] directions. When electric field is applied along [100] direction, $E_{\text{coer}}^{\text{Case1}} \approx E_{\text{coer}}^{\text{Case2}} > E_{\text{coer}}^{\text{Case3}}$. On the other hand, when electric field is applied along [001] direction, $E_{\text{coer}}^{\text{Case3}} > E_{\text{coer}}^{\text{Case1}} > E_{\text{coer}}^{\text{Case2}}$. Moreover, for the isotropic case (case 1, $Q_z = 1$), the difference in longitudinal and transverse E_{coer} values is the lowest. The difference in E_{coer} values is the largest for case 3 (showing three-phase coexistence) followed by case 2 (showing two-phase coexistence). Thus anisotropy in switching behavior increases with increasing electrostrictive anisotropy and decreasing polar anisotropy.

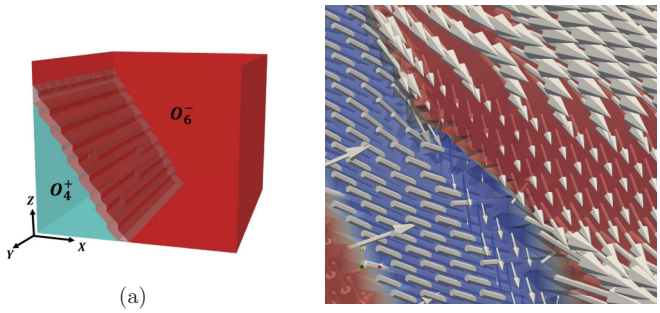

(a) (b)

FIG. 9. (a) *O*-*O* domain wall. (b) Formation of a step-terrace structure at the domain boundary.

The effective piezoelectric coefficients d_{33} and d_{31} for each case are obtained from the slopes of the linear portions of the corresponding butterfly loops. The computed values of effective d_{33}, d_{31}, and their ratio (d_{33}/d_{31}) for all cases are listed in Table II. The ratio (d_{33}/d_{31}) can be considered to be a response of electromechanical anisotropy resulting due to domain reorientation and inter-phase transition in these systems when subjected to external electro-mechanical load. From Table II we observe, among all the three cases, the largest anisotropy between the in-plane and out-of-plane response occurs for case 2 although Q_z is moderate ($Q_z = 2$). Also note that we assume $d_{33}/d_{31} = 1$ is the electromechanically isotropic case. However, while in case 3 (i.e., $Q_z = 2.5$) where several phases coexist (T, R, O) the electromechanical anisotropy is the lowest. Also note that, the domain morphology consisting of alternate layers of T and O lamellae (case 2), oriented nearly parallel to the Z axis contributes to the increase in electromechanical anisotropy. Thus we can ascertain that the distribution as well as the orientation of the domain morphologies play a substantial role in the alteration of the electromechanical anisotropy.

As we have already noted, number of phases increase with increasing Q_z. When the increase in the number of phases induces an increase in the number of distinct crystallographic variants, we generally expect enhancement in electromechanical response due to consequent increase in energetically favorable switching pathways. Therefore the $\bar{P}_z - E_3$ and $\bar{\varepsilon}_{33} - E_3$ loops corresponding to $Q_z = 2$ have the least width compared to $Q_z = 1, 2.5$ when the field is along [001] direction because the domain structure in the former contains the lowest number of distinct crystallographic variants ($n_{\text{var}} = 3$). However, electromechanical response also depends on the orientation of domain walls relative to the direction of applied switching field. Thus $\bar{P}_z - E_1$ and $\bar{\varepsilon}_{33} - E_1$ for $Q_z = 2$ shows the least width when the field is along [100].

In general, Figs. 11(a) and 11(b) show fatter $\bar{P}_z - E_3$, $\bar{\varepsilon}_{33} - E_3$ loops when electric field is applied along [001] direction. On the contrary, $\bar{P}_z - E_1$ and $\bar{\varepsilon}_{33} - E_1$ loops are narrower for all cases of Q_z when subjected to an electric field along [100] direction. This also indicates the difficulty in switching along the [001] direction.

The anisotropic nature of predicted hysteresis loops are commensurate with the underlying domain pattern and the domain wall structure for all cases of Q_z. Since the domain boundaries in equimolar BZCT have a strong ferroelastic nature, as evidenced by their step-terrace structure for all cases of Q_z, polarization reversal in each case happens via successive steps where the easy polarization rotation axes are determined by the orientation of step or terrace relative to

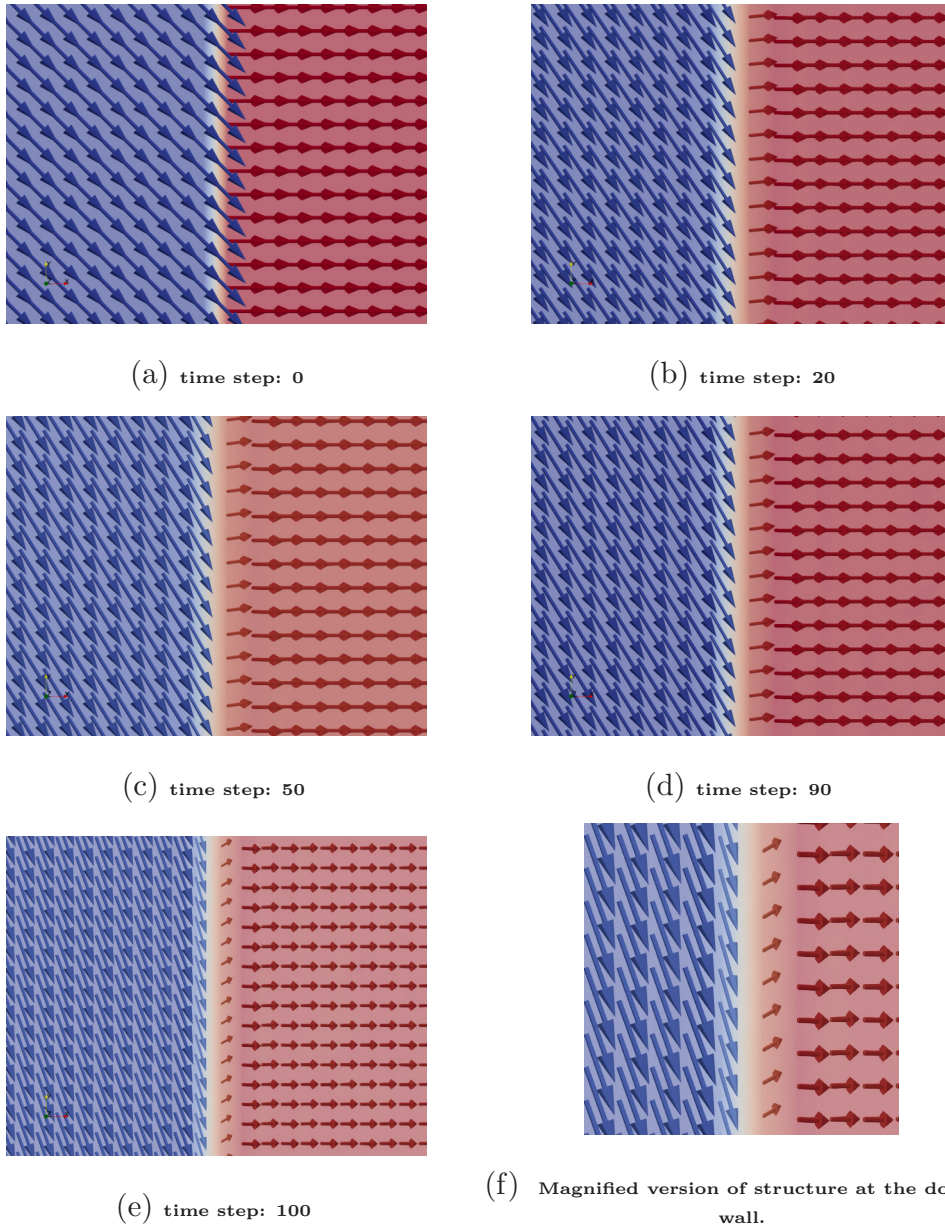

FIG. 10. Formation of the step-terrace structure at the domain wall. (a) Initial configuration of two domains $O_4^+[1\bar{1}0]$ (marked as blue) and $O_6^-[10\bar{1}]$ (marked as red) with sharp domain wall. [(b)–(e)] As the system evolves the domains reorient forming a step-terrace like pattern at the domain wall to maintain the proper head → tail configuration.

the direction of applied field (Fig. 8). Moreover, we find the aspect ratio between terrace (perpendicular to [001]) and step (parallel to [0 0 1]) to be greater than unity in all cases. This indicates a larger polarization component associated with the terrace that is normal to [001] than a step that is parallel to [100]. Therefore the energy required for polarization reversal is higher when the switching field is along [001] direction than it is along [100] direction. For a similar reason, strain associated with longitudinal strain hysteresis loop ($\bar{\varepsilon}_{33} - E_3$) is always larger than that associated with the transverse strain hysteresis loop ($\bar{\varepsilon}_{33} - E_1$).

Alternatively, one can explain the difference between d_{33} and d_{31} based on the energy barrier associated with switching. For example, in case 2, when we apply electric field along [001] direction, the system transforms to O_4^- from O_6^-. On the other hand, application of electric field along [100] direction switches the system to O_3^+. In Fig. 12, we show configuration energy (f_{conf}) (i.e., the energy required to switch the polarization variants with applied electric field) as a function of average polarization. The lower energy barrier for O_3^+ (blue line) clearly indicates that the switching from O_6^- to O_3^+ with applied electric field along [100] direction requires lower energy (easy polarization switching) compared to the other one (red line).

We also check the effective elastic moduli for all three cases where, we compare the elastic softening associated with

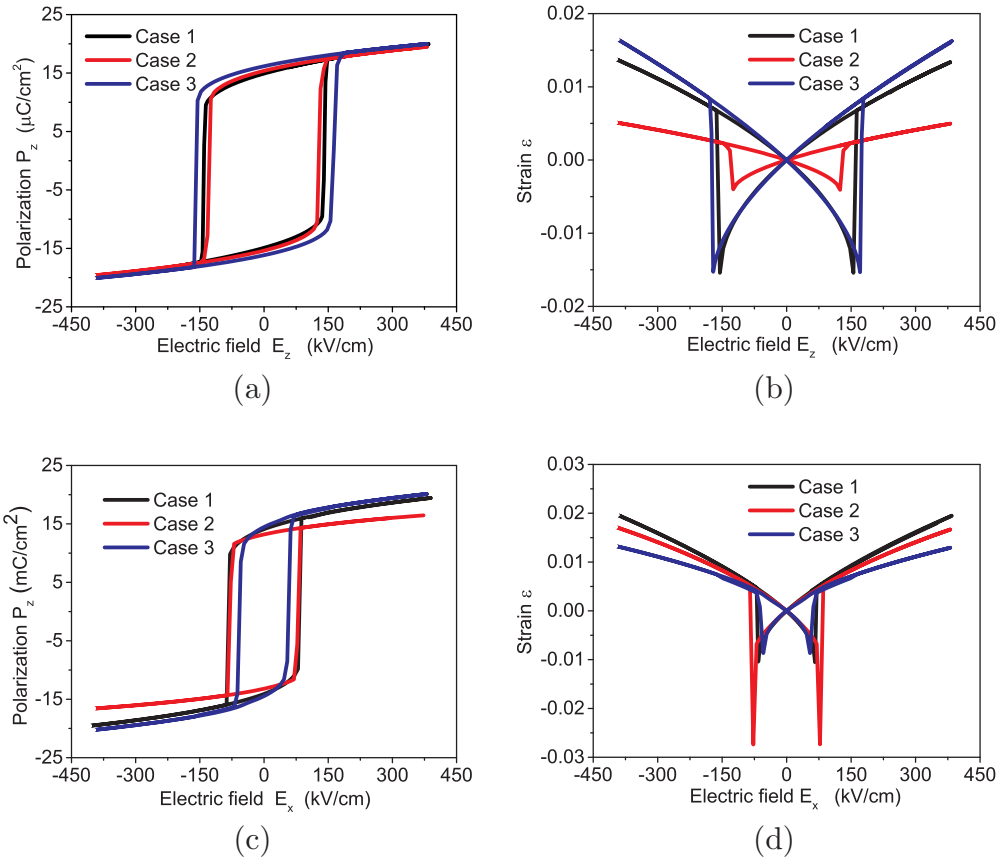

FIG. 11. Corresponding hysteresis and the butterfly loops for case 1 ($Q_z = 1$), case 2 ($Q_z = 2$), and case 3 ($Q_z = 2.5$). [(a) and (b)] Polarization and longitudinal strain hysteresis loops when applied electric field is along [001] direction. [(c) and (d)] Polarization and transverse strain hysteresis loops when applied electric field is along [100] direction.

phase coexistence. The effective elastic stiffness tensor C^{eff}_{ijkl} is obtained by measuring the stress response when the system is subjected to applied strain [63]. The effective elastic moduli corresponding to case 3 ($Q_z = 2.5$) show the lowest values among all cases indicating an increase in elastic softening with the increase in the number of crystallographically distinct variants.

Since our thermodynamic model includes elastic interactions, we can use the model to analyze phase stability in stress-free as well as mechanically constrained systems. When BZCT system with isotropic electrostrictive coefficients ($Q_z = 1$) is clamped in all directions (imposed by setting all components of homogeneous/macroscopic strain to be zero in the entire system), our model predicts change in room-temperature phase stability from orthorhombic (stress-free) to tetragonal (clamped) when the composition ranges between $0.49 \leqslant x \leqslant 0.53$, as shown in the free energy-composition diagrams of stress-free and constrained BZCT [Figs. 13(a) and 13(b)]. The simulated steady state domain structure of constrained equimolar BZCT at room temperature contains only tetragonal variants confirming our thermodynamic stability analysis for the mechanically constrained

TABLE II. d_{33}, d_{31}, and their ratio for the three cases.

	Case 1	Case 2	Case 3
$d_{33}(\text{pCN}^{-1})$	509	189	549
$d_{31}(\text{pCN}^{-1})$	798	727	680
d_{33}/d_{31}	0.64	0.26	0.81

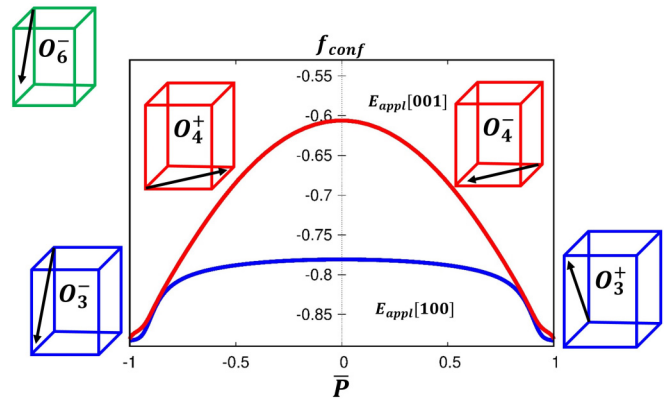

FIG. 12. (Case 2) Configuration energy (f_{conf}) as a function of average polarization. The green unit cell defines the initial O_6^- state before applying electric field. Application of electric field along [001] direction switches the system to O_4^- state as shown by the red unit cell. When the applied electric field is along [100] direction the system transforms to O_3^+ (shown by blue unit cell). The difference between the energy clearly indicates that the switching of O_3^+ from O_6^- is easier compared to O_4^-.

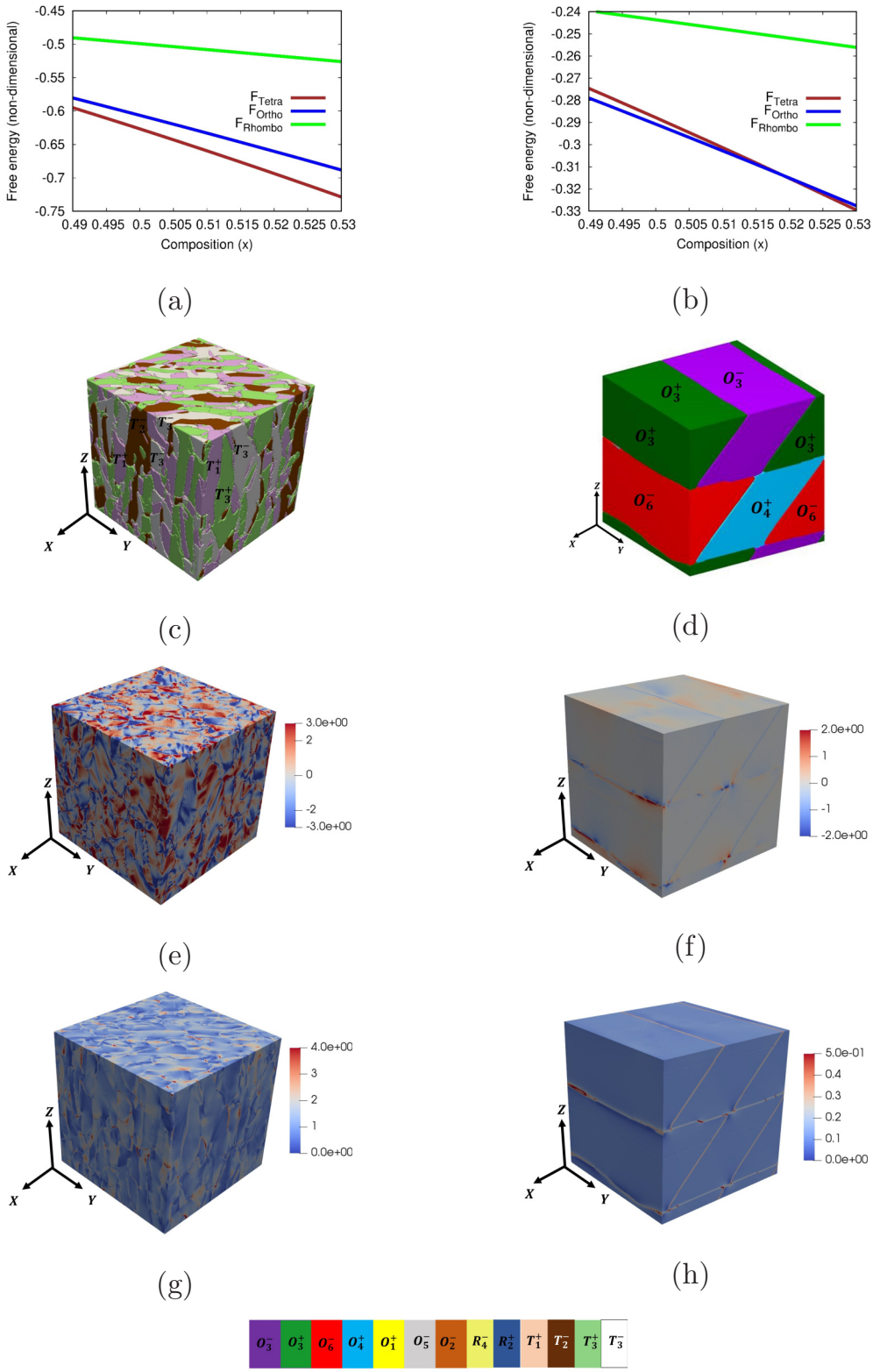

FIG. 13. Free energy - composition diagram of clamped BZCT system at room temperature indicating minimum free energy of the T phase between $0.49 \leqslant x \leqslant 0.53$. (b) Corresponding free energy-composition diagram of stress-free BZCT system at room temperature. Simulated steady state domain structures of equimolar BZCT at room temperature for (c) mechanically constrained and (d) stress-free conditions. Here $Q_z = 1$. [(e) and (f)] Electric energy distribution (nondimensional) corresponding to constrained and stress-free systems. [(g) and (h)] Elastic energy distribution (nondimensional) corresponding to constrained and stress-free systems. O_1^+ : [110], O_1^- : [$\bar{1}\bar{1}$0], O_2^+ : [011], O_2^- : [0$\bar{1}\bar{1}$], O_3^+ : [101], O_3^- : [$\bar{1}$0$\bar{1}$], O_4^+ : [1$\bar{1}$0], O_4^- : [$\bar{1}$10], O_5^+ : [0$\bar{1}$1], O_5^- : [01$\bar{1}$], O_6^+ : [$\bar{1}$01], O_6^- : [10$\bar{1}$], T_3^+ : [001], T_3^- : [00$\bar{1}$], T_1^+ : [100], T_2^- : [0$\bar{1}$0].

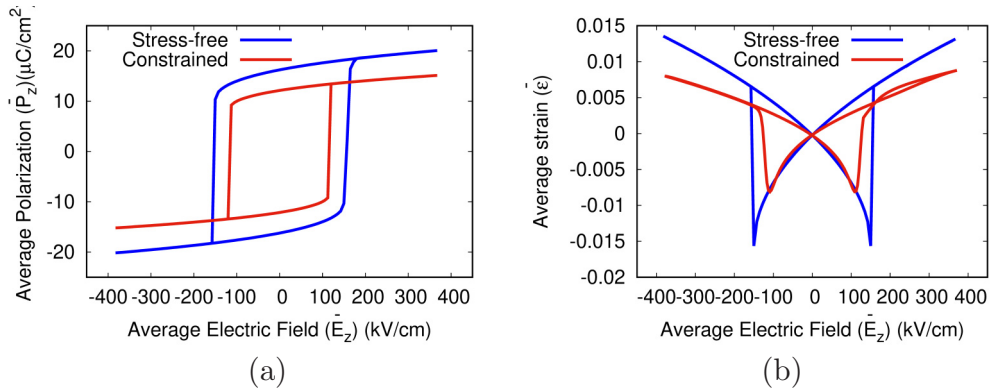

FIG. 14. (a) Polarization hysteresis and (b) strain hysteresis loops for mechanically constrained and stress-free BZCT. Constrained system shows narrower and thinner loops.

system [Fig. 13(c)]. The domain structure of constrained BZCT consists of thin stripes of T variants with curved domain walls, while the stress-free system possesses thicker and wider plates of O variants with straight boundaries. Although elastic interactions show a marked increase for the constrained system, electric interactions associated with both systems remain nearly the same [Figs. 13(e) and 13(g)]. The clamped system shows internal stress buildup given by $\bar{\sigma}_{ij} = q_{ijkl}\langle P_k P_l\rangle$. As a result, domain walls in this system show an increase in curvature.

The calculated polarization hysteresis loops ($\bar{P}_z - E_3$) and longitudinal strain hysteresis loops ($\epsilon_{33} - E_3$) for constrained and stress-free systems are shown in Fig. 14. The loops corresponding to the constrained system show lower E_{coer} value. The calculated effective d_{33} of 634 pCN^{-1} for the mechanically constrained system shows the closest match with the experimentally measured value ($d_{33}^{\text{exp}} = 620$ pC N^{-1} [25]). The close match between the constrained value and the experimental value points to the fact that all measurements are carried out in mechanically constrained conditions. Indeed it is difficult to maintain ideal stress-free conditions in any experimental setup that requires measurement of strain. Moreover, all simulated loops from our phase-field model show good agreement with with the analytically obtained hysteresis loops (Fig. 15) indicating thermodynamic consistency of our model.

Figure 16 shows the evolution of the clamped system when $Q_z = 1$. Here, we examine two different cases. First, a clamped system with initial random configuration [Fig. 16(a)]. The system evolves and transforms to a complete tetragonal (T) phase consisting of T_3^+, T_3^-, T_1^+ [Figs. 16(b)–16(d)] domains which is also shown in Fig. 13(c). On the other hand, we consider a system with the equilibrium steady state domain structure (case 1) [Fig. 16(d)]. Unlike the previous case the system equilibrates to a mixture of (T) and O domains as shown in Figs. 16(e) and 16(f). In this context, we can argue that in the previous case, as the system initiates with random thermal fluctuations, due to clamping, it spontaneously transforms to the tetragonal morphology. However, for the other case, the presence of clamping manifests metastable O phase coexisting along with the T phase.

IV. CONCLUSION

Our study presents a thermodynamic framework to predict process-structure-property relations in BZCT ceramics. The framework consists of a thermodynamic model coupled with phase-field simulations to analyze phase stability, domain structure evolution, and polarization switching propertiesof bulk ferroelectric solid solution (BZCT) containing a morphotropic phase coexistence region.

Changes in electromechanical processing conditions may induce structural changes in oxygen octahedra manifested

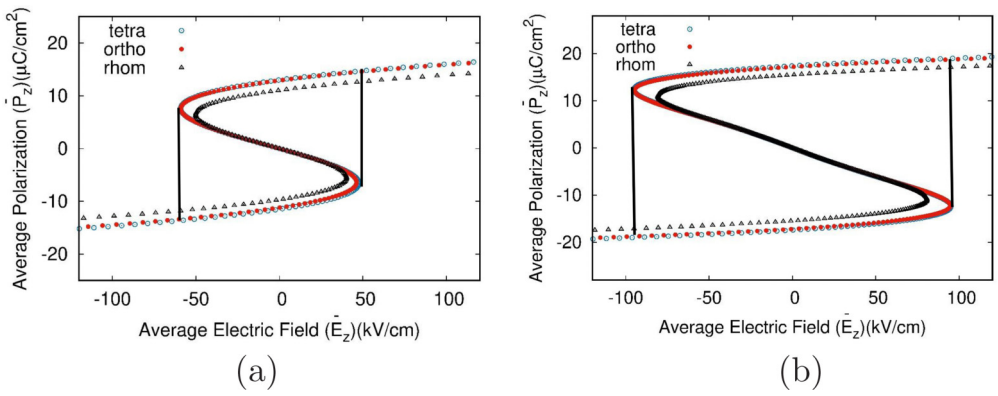

FIG. 15. Comparison between the analytical hysteresis loops for (a) constrained and (b) stress-free systems.

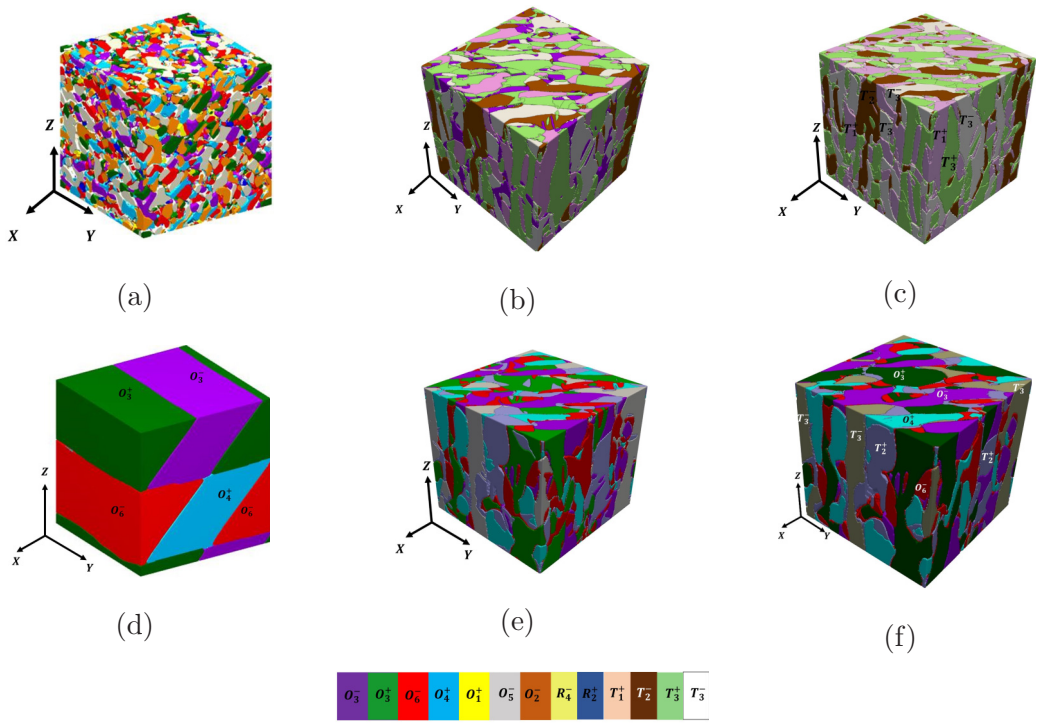

FIG. 16. Morphological evolution of the clamped system. (a) Initial random configuration. [(b) and (c)] Evolution of the domain morphologies with the random initial configuration resulting in the complete transformation of T phase. (d) Initial configuration (steady state domain morphology as obtained in a stress-free system). [(e) and (f)] Evolution of the domain morphologies indicating the coexistence of T & O phases (In all these cases $Q_z = 1$). $O_1^+ : [110]$, $O_1^- : [\bar{1}\bar{1}0]$, $O_2^+ : [011]$, $O_2^- : [0\bar{1}\bar{1}]$, $O_3^+ : [101]$, $O_3^- : [\bar{1}0\bar{1}]$, $O_4^+ : [1\bar{1}0]$, $O_4^- : [\bar{1}10]$, $O_5^+ : [0\bar{1}1]$, $O_5^- : [01\bar{1}]$, $O_6^+ : [\bar{1}01]$, $O_6^- : [10\bar{1}]$, $T_3^+ : [001]$, $T_3^- : [00\bar{1}]$, $T_1^+ : [100]$, $T_2^- : [0\bar{1}0]$.

by a change in anisotropy in electrostriction in the paraelectric state. Using our model we studied changes in ferroelectric domain stability as a function of electrostrictive anisotropy parameter Q_z. Our predictions of morphotropic phase boundaries and tricritical points show excellent agreement with experimental data obtained using high-resolution x-ray diffraction studies and Rietveld analysis [26,27]. The predicted diffusionless phase diagrams show a gradual change in phase stability within the morphotropic phase region from single-phase orthorhombic (O) to two-phase tetragonal-orthorhombic ($T + O$) coexistence to a stable multiphase mixture of tetragonal, rhombohedral and orthorhombic ($T + R + O$) polar phases at room temperature with a corresponding increase in Q_z from 1 to 2.5. In all cases, the domains of all polar phases exhibit twinned platelike morphology with the domain boundaries oriented along low-energy crystallographic directions. Moreover, the mobile domain walls show a step-terrace structure that facilitates polarization reversal via ferroelastic steps.

Electric fields along [001] and [100] directions were applied to study polarization switching characteristics in each case. The ratio of the longitudinal and transverse piezoelectric coefficients indicates the highest electromechanical anisotropy (ratio between d_{33}/d_{31}) for case 2 ($Q_z = 2$). Case 3 ($Q_z = 2.5$) posses the lowest value while case 1 ($Q_z = 1.0$) lies in between. The highest electromechanical anisotropy in case 2 is attributed to the alternating lamellae of the T and O domains with the domain wall orientation nearly parallel to the Z axis.

Further we show that electromechanical anisotropy (d_{33}/d_{31}) decreases with the decrease in polar anisotropy. Case 3 ($T + R + O$ coexistence) shows the lowest polar anisotropy as well as the lowest electromechanical anisotropy. On the other hand, case 2 ($T + O$) shows the highest polarization as well as electromechanical anisotropy since its domain configuration consists of the lowest number of polar variants. Although case 1 shows a single O phase, the number of variants of the O phase is larger than in case 2.

In addition to anisotropy in electrostriction, mechanical constraints can also modify phase stability bulk BZCT system. Thus, on the application of mechanical constraint to case 1, the thermodynamic stability changes from O to T at the equimolar composition at room temperature. Interestingly, d_{33} corresponding to the constrained system (634 pCN^{-1}) shows the closest match with the experimentally reported value [25].

ACKNOWLEDGMENTS

S.B., T.J., and S. Bhattacharyya gratefully acknowledge the support of DST (Grant No. EMR/2016/006007) for funding the computational research.

TABLE III. Relation between the original Landau coefficients and the modified ones

Unmodified coefficients	Modified coefficients
α_1	α_1
α_{12}	β_1
α_{11}	$\beta_1+\beta_2$
α_{112}	γ_1
α_{111}	$\gamma_1+\gamma_2$
α_{123}	$\gamma_3+6\gamma_1$

APPENDIX A: DERIVATION OF THE FREE ENERGY DENSITIES

Using 2-4-6 Ginzburg-Landau polynomial the bulk free energy density f_{bulk} for BZCT is expressed as

$$\begin{aligned} f_{\text{bulk}} &= \tfrac{1}{2}\alpha_1\left(P_1^2+P_2^2+P_3^2\right)+\tfrac{1}{4}\alpha_{11}\left(P_1^4+P_2^4+P_3^4\right)\\ &+\tfrac{1}{6}\alpha_{111}\left(P_1^6+P_2^6+P_3^6\right)+\tfrac{1}{2}\alpha_{12}\left(P_1^2P_2^2+P_2^2P_3^2+P_3^2P_1^2\right)\\ &+\tfrac{1}{2}\alpha_{112}\left(P_1^4\left(P_2^2+P_3^2\right)+P_2^4\left(P_3^2+P_1^2\right)+P_3^4\left(P_1^2+P_2^2\right)\right)\\ &+\tfrac{1}{6}\alpha_{123}P_1^2P_2^2P_3^2, \end{aligned} \tag{A1}$$

To derive thermodynamic stability conditions and compute diffusionless phase diagrams of BZCT system, Eq. (A1) is expressed in an alternate form based on polar anisotropy theory where we separate isotropic part of the free energy from the direction-dependent anisotropic part [37,41]. Therefore we define the spontaneous polarization field $\mathbf{P}$ as a product of the magnitude of spontaneous polarization $P=|\mathbf{P}|$ and a unit vector $\mathbf{n}=(n_1,n_2,n_3)$ along the direction of spontaneous polarization: $\mathbf{P}=\mathbf{n}P$. Thus Eq. (A1) becomes

$$\begin{aligned} f_{\text{bulk}}^{\text{modified}} &= \tfrac{1}{2}\alpha_1\left(n_1^2+n_2^2+n_3^2\right)P^2+\tfrac{1}{4}\alpha_{11}\left(n_1^4+n_2^4+n_3^4\right)P^4\\ &+\tfrac{1}{6}\alpha_{111}\left(n_1^6+n_2^6+n_3^6\right)P^6\\ &+\tfrac{1}{2}\alpha_{12}\left(n_1^2n_2^2+n_2^2n_3^2+n_3^2n_1^2\right)P^4+\tfrac{1}{2}\alpha_{112}\left(n_1^4\left(n_2^2+n_3^2\right)\right.\\ &\left.+n_2^4\left(n_3^2+n_1^3\right)+n_3^4\left(n_1^2+n_2^2\right)\right)P^6\\ &+\tfrac{1}{6}\alpha_{123}n_1^2n_2^2n_3^2P^6, \end{aligned} \tag{A2}$$

where $f_{\text{bulk}}^{\text{modified}}$ is the alternate form of the bulk free energy which separates isotropic and anisotropic contributions. Note that the isotropic part of the energy describes the transition from a nonpolar phase to a polar glassy state with no preferential direction, while the anisotropic part defines the directional dependence of free energy surface due to the spontaneous polarization vector [37,41]. The polar anisotropic contribution to the free energy is given by the cross terms of Eq. (A2). Since $(n_1^2+n_2^2+n_3^2)^m=1$ for any exponent m, the powers of the expansion terms in Eq. (A2) for $m=2,3$ can be written as

$$\left(n_1^2+n_2^2+n_3^2\right)^2=\left(n_1^4+n_2^4+n_3^4\right)+2\left(n_1^2n_2^2+n_2^2n_3^2+n_3^2n_1^2\right), \tag{A3a}$$

$$\begin{aligned} \left(n_1^2+n_2^2+n_3^2\right)^3 &= \left(n_1^6+n_2^6+n_3^6\right)+3\left(n_1^4\left(n_2^2+n_3^2\right)\right.\\ &\left.+n_2^4\left(n_3^2+n_1^2\right)+n_3^4\left(n_1^2+n_2^2\right)\right)+6n_1^2n_2^2n_3^2. \end{aligned} \tag{A3b}$$

Substituting the relations in Eq. (A3) in Eq (A2), the modified free energy becomes

$$\begin{aligned} f_{\text{bulk}}^{\text{modified}} &= \tfrac{1}{2}\alpha_1P^2+\tfrac{1}{4}\left(\alpha_{12}+\left(\alpha_{11}-\alpha_{12}\right)\left(n_1^4+n_2^4+n_3^4\right)\right)P^4\\ &+\tfrac{1}{6}\left(\alpha_{112}+\left(\alpha_{111}-\alpha_{112}\right)\left(n_1^6+n_2^6+n_3^6\right)\right)P^6\\ &+\tfrac{1}{6}\left(\alpha_{123}-6\alpha_{112}\right)n_1^2n_2^2n_3^2P^6. \end{aligned} \tag{A4}$$

Separating the isotropic and anisotropic parts, we rewrite the modified bulk free energy as

$$\begin{aligned} f_{\text{bulk}}^{\text{modified}} &= f_{\text{bulk}}^{\text{iso}}+f_{\text{bulk}}^{\text{aniso}}, \quad \text{where}\\ f_{\text{bulk}}^{\text{iso}} &= \tfrac{1}{2}\alpha_1P^2+\tfrac{1}{4}\beta_1P^4+\tfrac{1}{6}\gamma_1P^6,\\ f_{\text{bulk}}^{\text{aniso}} &= \tfrac{1}{4}\beta_2\left(n_1^4+n_2^4+n_3^4\right)P^4+\tfrac{1}{6}\left[\gamma_2\left(n_1^6+n_2^6+n_3^6\right)\right.\\ &\left.+\gamma_3n_1^2n_2^2n_3^2\right]P^6, \end{aligned} \tag{A5}$$

where $\beta_1=\alpha_{12}$, $\beta_2=\alpha_{11}-\alpha_{12}$, $\gamma_1=\alpha_{112}$, $\gamma_2=\alpha_{111}-\alpha_{112}$, and $\gamma_3=\alpha_{123}-6\alpha_{112}$ are the modified Landau coefficients. Table III lists the coefficients of unmodified LGD energy [Eq. (A1)] and the modified version of the energy [Eq. (A5)].

Assuming the paraelectric cubic state as the reference state, we use Eq. (A5) to define free energies of the paraelectric cubic phase $C(P=0)$ and the ferroelectric $T(n_1,n_2,n_3=\pm1,0,0)$, $O(n_1,n_2,n_3=\pm1/\sqrt{2},\pm1/\sqrt{2},0)$ and $R(n_1,n_2,n_3=\pm1/\sqrt{3},\pm1/\sqrt{3},\pm1/\sqrt{3})$ phases of stress-free BZCT as follows:

$$f_{\text{C}}^{\text{modified}}=0, \tag{A6a}$$

$$f_{\text{T}}^{\text{modified}}=\tfrac{1}{2}\alpha_1P^2+\tfrac{1}{4}(\beta_1+\beta_2)P^4+\tfrac{1}{6}(\gamma_1+\gamma_2)P^6, \tag{A6b}$$

$$f_{\text{O}}^{\text{modified}}=\tfrac{1}{2}\alpha_1P^2+\tfrac{1}{4}(2\beta_1+\beta_2)P^4+\tfrac{1}{24}(4\gamma_1+\gamma_2)P^6, \tag{A6c}$$

$$\begin{aligned} f_{\text{R}}^{\text{modified}} &= \tfrac{1}{2}\alpha_1P^2+\tfrac{1}{12}(3\beta_1+\beta_2)P^4\\ &+\tfrac{1}{162}(27\gamma_1+3\gamma_2+\gamma_3)P^6. \end{aligned} \tag{A6d}$$

Minimization of Eqs. (A6b)–(A6d) with respect to P yields equilibrium spontaneous polarization $P_{s,\phi};\phi=T,O,R$ of the ferroelectric phases, T, O, and R as a function of temperature and composition:

$$P_{s,T}^2=\frac{1}{2}\frac{-(\beta_1+\beta_2)\pm\sqrt{(\beta_1+\beta_2)^2-4\alpha_1(\gamma_1+\gamma_2)}}{\gamma_1+\gamma_2}, \tag{A7a}$$

$$P_{s,O}^2=\frac{-(2\beta_1+\beta_2)\pm\sqrt{(2\beta_1+\beta_2)^2-4\alpha_1(4\gamma_1+\gamma_2)}}{4\gamma_1+\gamma_2}, \tag{A7b}$$

$$P_{s,R}^2=\frac{3}{2}\frac{-(9\beta_1+3\beta_2)\pm\sqrt{(9\beta_1+3\beta_2)^2-12\alpha_1(27\gamma_1+3\gamma_2+\gamma_3)}}{27\gamma_1+3\gamma_2+\gamma_3}. \tag{A7c}$$

The equilibrium free energies of T, O and R in terms of temperature and composition are obtained by substituting the expressions of spontaneous polarization of these phases [Eq. (A7)] in Eq (A6).

APPENDIX B: ORIENTATION DEPENDENCE OF FOURTH-ORDER ELECTROSTRICTIVE TENSOR IN TWO AND THREE DIMENSIONS

The relation between strain tensor and electric polarization can be written as $\epsilon_{ij} = s_{ijmn}q_{mnkl}P_kP_l = Q_{ijkl}P_kP_l$, where s_{ijkl} is the elastic compliance tensor, q_{ijkl} is the electrostrictive constant tensor, and Q_{ijkl} is the experimentally obtained electrostrictive coefficient tensor [31,36].

Following Nye [32], one can use a representation surface to observe the variation in electrostrictive modulus $(1/Q^*_{33})$ with the direction of applied electric field or electric polarization. Let us imagine a crystal to be cut with the length parallel to some arbitrary direction Z' with applied field along the reference [001] direction. Since Z' need not be parallel to [001], the applied field along [001] not only produces longitudinal and lateral strains but also shear. Thus Q^*_{33} along the direction of the applied field is given as the ratio between the longitudinal strain and the square of electric polarization along the direction of applied field. For a general anisotropic material, the electrostrictive modulus can be computed for general choices of crystallographic directions. Thus, for a cubic crystal, assuming the "old" axes to be orthonormal and aligned with respect to the ⟨100⟩ directions, for any arbitrary orthogonal transformation of coordinates from X, Y, Z to X', Y', Z', the electrostrictive modulus can be derived as

$$\frac{1}{Q^*_{33}} = \frac{(Q_{11}+Q_{12})}{(Q_{11}-Q_{12})(Q_{11}+2Q_{12})} - \frac{2Q_{44}-Q_{11}+Q_{12}}{Q_{44}(Q_{11}-Q_{12})}\left(l_1^2l_2^2+l_2^2l_3^2+l_3^2l_1^2\right), \quad \text{(B1)}$$

where l_1, l_2, l_3 are the direction cosines.

In this present work, we define the anisotropy in the electrostriction using a parameter $Q_z = \frac{2Q_{44}}{(Q_{11}-Q_{12})}$. This definition is analogous to the Zener anisotropy parameter used to describe anisotropy in elastic constants in cubic crystals. Equation (B1) in terms of Q_z can be written as

$$\frac{1}{Q^*_{33}} = \frac{(Q_{11}+Q_{12})}{(Q_{11}-Q_{12})(Q_{11}+2Q_{12})} - \frac{2Q_z-1}{Q_z(Q_{11}-Q_{12})}\left(l_1^2l_2^2+l_2^2l_3^2+l_3^2l_1^2\right). \quad \text{(B2)}$$

[1] Y. Saito, H. Takao, T. Tani, T. Nonoyama, K. Takatori, T. Homma, T. Nagaya, and M. Nakamura, Lead-free piezoceramics, Nature (London) **432**, 84 (2004).

[2] T. R. Shrout and S. J. Zhang, Lead-free piezoelectric ceramics: Alternatives for PZT?, J. Electroceramics **19**, 113 (2007).

[3] P. Panda and B. Sahoo, PZT to lead free piezo ceramics: A review, Ferroelectrics **474**, 128 (2015).

[4] H. He, X. Lu, E. Hanc, C. Chen, H. Zhang, and L. Lu, Advances in lead-free pyroelectric materials: A comprehensive review, J. Mater. Chem. C **8**, 1494 (2020).

[5] Y. Doshida, S. Kishimoto, K. Ishii, H. Kishi, H. Tamura, Y. Tomikawa, and S. Hirose, Miniature cantilever-type ultrasonic motor using Pb-free multilayer piezoelectric ceramics, Jpn. J. Appl. Phys. **46**, 4921 (2007).

[6] T. Tou, Y. Hamaguti, Y. Maida, H. Yamamori, K. Takahashi, and Y. Terashima, Properties of $(Bi_{0.5}Na_{0.5})TiO_3-BaTiO_3-(Bi_{0.5}Na_{0.5})(Mn_{1/3}Nb_{2/3})O_3$ lead-free piezoelectric ceramics and its application to ultrasonic cleaner, Jpn. J. Appl. Phys. **48**, 07GM03 (2009).

[7] Y. Doshida, H. Shimizu, Y. Mizuno, and H. Tamura, Investigation of high-power properties of (Bi, Na, Ba) TiO_3 and (Sr, Ca) $2NaNb_5O_{15}$ piezoelectric ceramics, Jpn. J. Appl. Phys. **52**, 07HE01 (2013).

[8] J. Rödel, W. Jo, K. T. Seifert, E.-M. Anton, T. Granzow, and D. Damjanovic, Perspective on the development of lead-free piezoceramics, J. Am. Ceram. Soc. **92**, 1153 (2009).

[9] D. G. Schlom, L.-Q. Chen, C.-B. Eom, K. M. Rabe, S. K. Streiffer, and J.-M. Triscone, Strain tuning of ferroelectric thin films, Annu. Rev. Mater. Res. **37**, 589 (2007).

[10] V. Buscaglia and C. A. Randall, Size and scaling effects in barium titanate. An overview, J. Eur. Ceram. Soc. **40**, 3744 (2020).

[11] Z. Yu, C. Ang, R. Guo, and A. Bhalla, Piezoelectric and strain properties of Ba $(Ti_{1-x}Zr_x)O_3$ ceramics, J. Appl. Phys. **92**, 1489 (2002).

[12] A. K. Kalyani, K. Brajesh, A. Senyshyn, and R. Ranjan, Orthorhombic-tetragonal phase coexistence and enhanced piezo-response at room temperature in Zr, Sn, and Hf modified $BaTiO_3$, Appl. Phys. Lett. **104**, 252906 (2014).

[13] W. Liu and X. Ren, Large piezoelectric effect in Pb-free ceramics, Phys. Rev. Lett. **103**, 257602 (2009).

[14] M. Acosta, N. Novak, W. Jo, and J. Rödel, Relationship between electromechanical properties and phase diagram in the $Ba(Zr_{0.2}Ti_{0.8})O_3$–$x(Ba_{0.7}Ca_{0.3})TiO_3$ lead-free piezoceramic, Acta Mater. **80**, 48 (2014).

[15] D. R. Brandt, M. Acosta, J. Koruza, and K. G. Webber, Mechanical constitutive behavior and exceptional blocking force of lead-free BZT-xBCT piezoceramics, J. Appl. Phys. **115**, 204107 (2014).

[16] H. Bao, C. Zhou, D. Xue, J. Gao, and X. Ren, A modified lead-free piezoelectric BZT–xBCT system with higher T_c, J. Phys. D: Appl. Phys. **43**, 465401 (2010).

[17] H. Khassaf, N. Khakpash, F. Sun, N. Sbrockey, G. Tompa, T. Kalkur, and S. Alpay, Strain engineered barium strontium titanate for tunable thin film resonators, Appl. Phys. Lett. **104**, 202902 (2014).

[18] V. Buscaglia, S. Tripathi, V. Petkov, M. Dapiaggi, M. Deluca, A. Gajović, and Y. Ren, Average and local atomic-scale structure in $BaZr_xTi_{1-x}O_3$ ($x = 0.10, 0.20, 0.40$) ceramics by high-energy x-ray diffraction and raman spectroscopy, J. Phys.: Condens. Matter **26**, 065901 (2014).

[19] B. Noheda, D. Cox, G. Shirane, J. Gonzalo, L. Cross, and S. Park, A monoclinic ferroelectric phase in the $Pb(Zr_{1-x}Ti_x)O_3$ solid solution, Appl. Phys. Lett. **74**, 2059 (1999).

[20] B. Noheda, D. E. Cox, G. Shirane, R. Guo, B. Jones, and L. E. Cross, Stability of the monoclinic phase in the ferroelectric perovskite $Pb(Zr_{1-x}Ti_x)O_3$, Phys. Rev. B **63**, 014103 (2000).

[21] B. Noheda, J. A. Gonzalo, L. E. Cross, R. Guo, S.-E. Park, D. E. Cox, and G. Shirane, Tetragonal-to-monoclinic phase transition in a ferroelectric perovskite: The structure of $PbZr_{0.52}Ti_{0.48}O_3$, Phys. Rev. B **61**, 8687 (2000).

[22] D. Cox, B. Noheda, G. Shirane, Y. Uesu, K. Fujishiro, and Y. Yamada, Universal phase diagram for high-piezoelectric perovskite systems, Appl. Phys. Lett. **79**, 400 (2001).

[23] S. Zhang, F. Li, X. Jiang, J. Kim, J. Luo, and X. Geng, Advantages and challenges of relaxor-$PbTiO_3$ ferroelectric crystals for electroacoustic transducers–a review, Prog. Mater. Sci. **68**, 1 (2015).

[24] A. Boutarfaia, C. Boudaren, A. Mousser, and S. Bouaoud, Study of phase transition line of PZT ceramics by x-ray diffraction, Ceram. Int. **21**, 391 (1995).

[25] D. S. Keeble, F. Benabdallah, P. A. Thomas, M. Maglione, and J. Kreisel, Revised structural phase diagram of $(Ba_{0.7}Ca_{0.3}TiO_3)$-$(Bazr_{0.2}Ti_{0.8}O_3)$, Appl. Phys. Lett. **102**, 092903 (2013).

[26] K. Brajesh, K. Tanwar, M. Abebe, and R. Ranjan, Relaxor ferroelectricity and electric-field-driven structural transformation in the giant lead-free piezoelectric (Ba, Ca)(Ti, Zr)O_3, Phys. Rev. B **92**, 224112 (2015).

[27] K. Brajesh, M. Abebe, and R. Ranjan, Structural transformations in morphotropic-phase-boundary composition of the lead-free piezoelectric system $Ba(Ti_{0.8}Zr_{0.2})O_3$-$(Ba_{0.7}Ca_{0.3})TiO_3$, Phys. Rev. B **94**, 104108 (2016).

[28] A. Reyes-Montero, F. Rubio-Marcos, L. E. Fuentes-Cobas, A. Del Campo, R. Castañeda-Guzmán, M. E. Villafuerte-Castrejón, and L. Pardo, Confocal raman microscopy, synchrotron x-ray diffraction, and photoacoustic study of $Ba_{0.85}Ca_{0.15}Ti_{0.90}Zr_{0.10}O_3$: Understanding structural and microstructural response to the electric field, ACS Appl. Elec. Mater. **3**, 2966 (2021).

[29] F. Li, L. Jin, Z. Xu, and S. Zhang, Electrostrictive effect in ferroelectrics: An alternative approach to improve piezoelectricity, Appl. Phys. Rev. **1**, 011103 (2014).

[30] M. E. Lines and A. M. Glass, *Principles and Applications of Ferroelectrics and Related Materials* (Clarendon Press, Oxford, 1977).

[31] R. E. Newnham, *Properties of Materials: Anisotropy, Symmetry, Structure* (Oxford University Press, New York, 2005).

[32] J. F. Nye, *Physical Properties of Crystals* (Clarendon Press, Oxford, 1985).

[33] M. Budimir, D. Damjanovic, and N. Setter, Piezoelectric anisotropy–phase transition relations in perovskite single crystals, J. Appl. Phys. **94**, 6753 (2003).

[34] D. Damjanovic, Comments on origins of enhanced piezoelectric properties in ferroelectrics, IEEE Trans. Ultrason. Ferroelectr. Freq. Control **56**, 1574 (2009).

[35] M. Iwata, H. Orihara, and Y. Ishibashi, Anisotropy of piezoelectricity near morphotropic phase boundary in perovskite-type oxide ferroelectrics, Ferroelectrics **266**, 57 (2002).

[36] L.-Q. Chen, Phase-field method of phase transitions/domain structures in ferroelectric thin films: A review, J. Am. Ceram. Soc. **91**, 1835 (2008).

[37] A. A. Heitmann and G. A. Rossetti Jr, Thermodynamics of ferroelectric solid solutions with morphotropic phase boundaries, J. Am. Ceram. Soc. **97**, 1661 (2014).

[38] W. Cao and L. E. Cross, Theoretical model for the morphotropic phase boundary in lead zirconate–lead titanate solid solution, Phys. Rev. B **47**, 4825 (1993).

[39] A. J. Bell and E. Furman, A two-parameter thermodynamic model for PZT, Ferroelectrics **293**, 19 (2003).

[40] Y. Li, S. Hu, and L. Chen, Ferroelectric domain morphologies of (001) $PbZr_{1-x}Ti_xO_3$ epitaxial thin films, J. Appl. Phys. **97**, 034112 (2005).

[41] A.A. Heitmann and G. Rossetti Jr, Thermodynamics of polar anisotropy in morphotropic ferroelectric solid solutions, Philos. Mag. Lett. **90**, 71 (2010).

[42] T. Yang, X. Ke, and Y. Wang, Mechanisms responsible for the large piezoelectricity at the tetragonal-orthorhombic phase boundary of $(1-x)BaZr_{0.2}Ti_{0.8}O_3$-$xBa_{0.7}Ca_{0.3}TiO_3$ system, Sci. Rep. **6**, 1 (2016).

[43] Y. H. Huang, J.-J. Wang, T. N. Yang, X. X. Cheng, B. Liu, Y. J. Wu, and L.-Q. Chen, Thermodynamic and phase-field studies of phase transitions, domain structures, and switching for Ba$(Zr_xTi_{1-x})O_3$ solid solutions, Acta Mater. **186**, 609 (2020).

[44] J. Hlinka and P. Marton, Phenomenological model of a 90^0 domain wall in $BaTiO_3$-type ferroelectrics, Phys. Rev. B **74**, 104104 (2006).

[45] S. Wang, M. Yi, and B.-X. Xu, A phase-field model of relaxor ferroelectrics based on random field theory, Int. J. Solids Struct. **83**, 142 (2016).

[46] A. K. Tagantsev, Landau expansion for ferroelectrics: Which variable to use?, Ferroelectrics **375**, 19 (2008).

[47] A. P. Levanyuk, B. A. Strukov, and A. Cano, Background dielectric permittivity: Material constant or fitting parameter?, Ferroelectrics **503**, 94 (2016).

[48] C. Woo and Y. Zheng, Depolarization in modeling nano-scale ferroelectrics using the Landau free energy functional, Appl. Phys. A **91**, 59 (2008).

[49] A. G. Khachaturyan and G. A. Shatalov, periodicity for a phase transition in solid state, Sov. Phys. JETP **29**, 557 (1969).

[50] A. Lubk, S. Gemming, and N. A. Spaldin, First-principles study of ferroelectric domain walls in multiferroic bismuth ferrite, Phys. Rev. B **80**, 104110 (2009).

[51] Y. Wang, C. Nelson, A. Melville, B. Winchester, S. Shang, Z.-K. Liu, D. G. Schlom, X. Pan, and L.-Q. Chen, $BiFeO_3$ domain wall energies and structures: A combined experimental and density functional theory + U study, Phys. Rev. Lett. **110**, 267601 (2013).

[52] F. Xue, Y. Gu, L. Liang, Y. Wang, and L.-Q. Chen, Orientations of low-energy domain walls in perovskites with oxygen octahedral tilts, Phys. Rev. B **90**, 220101(R) (2014).

[53] P. Chandra and P. B. Littlewood, A Landau primer for ferroelectrics, in *Physics of Ferroelectrics: A Modern Perspective* (Springer, Berlin, Heidelberg, 2007), pp. 69–116.

[54] L. Q. Chen, J. Shen *et al.*, Applications of semi-implicit fourier-spectral method to phase-field equations, Comput. Phys. Commun. **108**, 147 (1998).

[55] A. Turygin, M. Neradovskiy, N. Naumova, D. Zayats, I. Coondoo, A. Kholkin, and V. Y. Shur, Domain structures and local switching in lead-free piezoceramics $Ba_{0.85}Ca_{0.15}Ti_{0.90}Zr_{0.10}O_3$, J. Appl. Phys. **118**, 072002 (2015).

[56] P. Marton and J. Hlinka, Simulation of domain patterns in $BaTiO_3$, Phase Transit. **79**, 467 (2006).

[57] D. Xue, Y. Zhou, H. Bao, C. Zhou, J. Gao, and X. Ren, Elastic, piezoelectric, and dielectric properties of $Ba(Zr_{0.2}Ti_{0.8})O_3$-$50(Ba_{0.7}Ca_{0.3})TiO_3$ Pb-free ceramic at the morphotropic phase boundary, J. Appl. Phys. **109**, 054110 (2011).

[58] See Supplemental Material at http://link.aps.org/supplemental/10.1103/PhysRevB.108.134116 for information regarding the dimensional as well as nondimensional forms of the composition and temperature dependent parameters used in the study. It also provides information regarding the calculation of the angle between the steps and terraces in a representative step-terrace morphology.

[59] T. Yamada, Electromechanical properties of oxygen-octahedra ferroelectric crystals, J. Appl. Phys. **43**, 328 (1972).

[60] D. Damjanovic, Contributions to the piezoelectric effect in ferroelectric single crystals and ceramics, J. Am. Ceram. Soc. **88**, 2663 (2005).

[61] L. Zhang, M. Zhang, L. Wang, C. Zhou, Z. Zhang, Y. Yao, L. Zhang, D. Xue, X. Lou, and X. Ren, Phase transitions and the piezoelectricity around morphotropic phase boundary in $Ba(Zr_{0.2}Ti_{0.8})O_3$-$x(Ba_{0.7}Ca_{0.3})TiO_3$ lead-free solid solution, Appl. Phys. Lett. **105**, 162908 (2014).

[62] R. Xu, S. Liu, I. Grinberg, J. Karthik, A. R. Damodaran, A. M. Rappe, and L. W. Martin, Ferroelectric polarization reversal via successive ferroelastic transitions, Nat. Mater. **14**, 79 (2015).

[63] S. Bhattacharyya, T. W. Heo, K. Chang, and L.-Q. Chen, A spectral iterative method for the computation of effective properties of elastically inhomogeneous polycrystals, Commun. Comput. Phys. **11**, 726 (2012).